

# Atomistic Insights into Lithium Storage Mechanisms in Anatase, Rutile, and Amorphous TiO<sub>2</sub> Electrodes

Jodie A. Yuwono,\* Patrick Burr, Conor Galvin, and Alison Lennon

Cite This: <https://dx.doi.org/10.1021/acsami.0c17097>

Read Online

ACCESS |



Metrics &amp; More



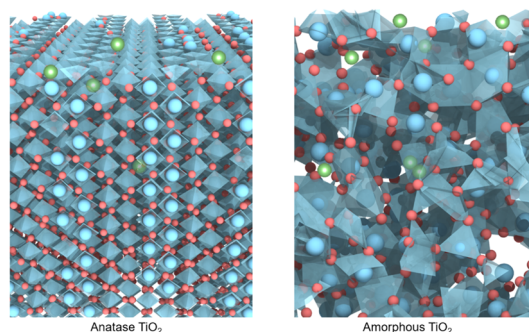
Article Recommendations



Supporting Information

**ABSTRACT:** Density functional theory calculations were used to investigate the phase transformations of Li<sub>x</sub>TiO<sub>2</sub> (at 0 ≤ x ≤ 1), solid-state Li<sup>+</sup> diffusion, and interfacial charge-transfer reactions in both crystalline and amorphous forms of TiO<sub>2</sub>. It is shown that in contrast to crystalline TiO<sub>2</sub> polymorphs, the energy barrier to Li<sup>+</sup> diffusion in amorphous TiO<sub>2</sub> decreases with increasing mole fraction of Li<sup>+</sup> due to the changes of chemical species pair interactions following the progressive filling of low-energy Li<sup>+</sup> trapping sites. Sites with longer Li–Ti and Li–O interactions exhibit lower Li<sup>+</sup> insertion energies and higher migration energy barriers. Due to its disordered atomic arrangement and increasing Li<sup>+</sup> diffusivity at higher mole fractions, amorphous TiO<sub>2</sub> exhibits both surface and bulk storage mechanisms. The results suggest that nanostructuring of crystalline TiO<sub>2</sub> can increase both the rate and capacity because the capacity dependence on the bulk storage mechanism is minimized and replaced with the surface storage mechanism. These insights into Li<sup>+</sup> storage mechanisms in different forms of TiO<sub>2</sub> can guide the fabrication of TiO<sub>2</sub> electrodes to maximize the capacity and rate performance in the future.

**KEYWORDS:** titanium dioxide, amorphous, anatase, rutile, lithium-ion batteries, anode, density functional theory

Atomic Scale Mechanisms of Li<sup>+</sup> Insertion and Diffusion in Crystalline and Amorphous TiO<sub>2</sub>

## 1. INTRODUCTION

Next-generation electrochemical energy storage systems with high-rate capability are of great interest for electric vehicles and renewable energy systems.<sup>1,2</sup> Lithium-ion batteries (LIBs) are promising candidates; however, the use of high charging rates (C-rates larger than 1 C) with the commonly used graphite anodes can lead to increased battery impedance and introduce safety concerns due to the formation of Li dendrites.<sup>3,4</sup> Graphite has a low lithiation potential (~0.1 V vs Li<sup>+</sup>/Li), and consequently, large overpotentials induced at high current densities can result in plating of Li on the anode surface.<sup>5,6</sup> Furthermore, if the overpotential is non-uniform across the surface, then, Li dendritic structures can grow and subsequently lead to a battery short circuiting and, in worst cases, cause fires. A strategy for high-rate LIBs is to use anode materials with a higher lithiation potential. One such anode material is lithium titanium oxide in the spinel form (LTO, Li<sub>4</sub>Ti<sub>5</sub>O<sub>12</sub>) which has a lithiation potential of ~1.5 V versus Li<sup>+</sup>/Li.<sup>7,8</sup> In general, the use of high-potential anodes in LIBs results in a lower energy density; however, the decrease in energy density is compensated by increased safety (i.e., a reduced risk of Li plating), greater retention of capacity at higher rates (i.e., increased power), and longer battery cycling [i.e., reduced electrolyte reduction to form a solid electrolyte interface (SEI) and cause electrolyte depletion]. The capacity

of spinel LTO can remain stable at 124 mA h g<sup>-1</sup> when charged and discharged at a rate of 50 C for 3000 cycles.<sup>9</sup>

Various crystalline TiO<sub>2</sub> polymorphs (e.g., rutile, anatase, brookite, and bronze) have also been investigated as alternatives to LTO as a LIB anode material.<sup>10–13</sup> Titanium dioxide has a theoretical capacity of 335 mA h g<sup>-1</sup> or 1280 mA h cm<sup>-3</sup>, which corresponds to the accommodation of one Li ion in one TiO<sub>2</sub> formula unit. Bulk crystalline TiO<sub>2</sub> exhibits poor ionic and electronic conductivities; therefore, it is necessary to use electrode doping strategies<sup>14–16</sup> and/or nanoarchitectures (e.g., nanotubes, nanomembranes, nanopillars, and so forth)<sup>17–22</sup> to increase lithiation capacity at high rates. Nanoarchitecture electrodes, such as nanotube arrays and thin films with a thickness in the order of nanometers, exhibit reduced phase segregation and reduced electrode structural change during cycling,<sup>23–27</sup> suggesting that Li<sup>+</sup> insertion in TiO<sub>2</sub> is driven by a competition between the solid solution and phase segregation. Despite the recent advances in fabricating nanoscale TiO<sub>2</sub>-based anodes, there

**Received:** September 22, 2020

**Accepted:** December 22, 2020

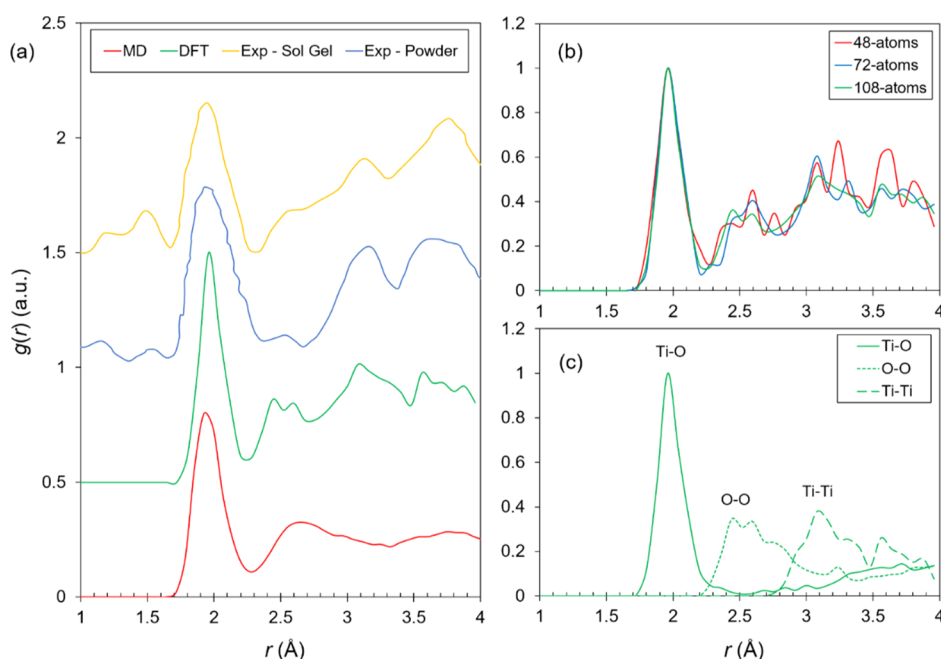


**Figure 1.** (a) Radial distribution function of amorphous  $\text{TiO}_2$  as obtained from atomic simulations (MD and DFT) compared with distributions obtained from XRD analysis of thin  $\text{TiO}_2$  films.<sup>58</sup> (b) Amorphous  $\text{TiO}_2$   $g(r)$  obtained using DFT with different supercell sizes and (c)  $g(r)$  of a 108-atom supercell broken down into contributions from pairs of chemical species: Ti–O, O–O, and Ti–Ti.

remains an incomplete understanding of the atomic-scale mechanisms associated with  $\text{Li}^+$  storage in these materials. The investigations reported in this paper shed light on the contributions of surface and bulk  $\text{Li}^+$  insertion, especially during the early stage of lithiation in different  $\text{TiO}_2$  polymorphs.

Crystal structure also determines the rate of  $\text{Li}^+$  migration in  $\text{TiO}_2$ . Faster lithiation in *bronze*  $\text{TiO}_2$  compared with anatase originates from the presence of open and freely accessible parallel channels on the surface.<sup>19,28</sup> Amorphous metal oxide, including  $\text{TiO}_2$ , has recently received increasing attention due to its open structure to accommodate  $\text{Li}^+$ ,<sup>29,30</sup> and higher capacities and rate capabilities have been reported for amorphous  $\text{TiO}_2$  compared to crystalline  $\text{TiO}_2$ .<sup>31,32</sup> Broad lithiation and de-lithiation peaks, resembling more capacitive storage, are observed in cyclic voltammetry (CV) measurements involving amorphous  $\text{TiO}_2$  electrodes. These broader peaks are more evident with amorphous  $\text{TiO}_2$  nano-sized structures, which possess more free space on the surface in addition to the open spatial channels in the bulk.<sup>33,34</sup> Jiang et al. reported that  $\text{Li}^+$  diffusion in amorphous  $\text{TiO}_2$  nanotubes is 2 orders of magnitude faster than that in anatase  $\text{TiO}_2$  nanotubes.<sup>32</sup> This observation was attributed to a combination of increased charge-transfer and  $\text{Li}^+$  diffusion rates in the amorphous material. Moitzheim et al. proposed an alternative lithiation mechanism for amorphous  $\text{TiO}_2$  based on a consideration of electronic and ionic conductivities.<sup>27</sup> Since amorphous  $\text{TiO}_2$  was assumed to have lower electronic conductivity<sup>35</sup> (because of increased electronic scattering) and higher ionic conductivity, the charge transfer was expected to occur in the bulk region, resulting in lithiation following a “bottom-up” mechanism. However, in anatase  $\text{TiO}_2$ , lithiation follows a “top-down” mechanism since a relatively faster electronic conductivity allows the reduction of  $\text{Ti}^{4+}$  to occur in the surface region. However, it is important to note that  $\text{Li}^+$  insertion and extraction are not limited by electronic and/or

ionic conductivity alone. It is possible that the decrease of electronic conductivity and the increase of ionic conductivity in amorphous  $\text{TiO}_2$  are not sufficiently large to make electronic conductivity the rate-limiting step for the charge-transfer reaction.

While the crystal structures of anatase and rutile  $\text{TiO}_2$  are well known, the structure of amorphous  $\text{TiO}_2$  remains difficult to be modeled. Considering the potential of amorphous  $\text{TiO}_2$  to be used for many applications (e.g., electrode materials for LIBs and photocatalytic and sensing materials), it is important to develop an accurate atomic model to improve understanding of the lithiation and de-lithiation processes in this material. In the present study, atomic simulations were used to develop an atomistic model of amorphous  $\text{TiO}_2$ . The developed model was then used to investigate  $\text{Li}^+$  insertion, extraction, and diffusion in amorphous and crystalline anatase and rutile  $\text{TiO}_2$ . The estimation of interfacial and bulk diffusion of  $\text{Li}^+$  in  $\text{TiO}_2$ , which are difficult to probe from experiments, was investigated individually here. A fundamental mechanistic difference between the insertion and extraction of  $\text{Li}^+$  between amorphous and crystalline  $\text{TiO}_2$  was identified, providing insights for rationalizing their different lithiation and de-lithiation behaviors as anodes for LIBs for high-rate and high-capacity applications.

## 2. METHODS

Amorphous  $\text{TiO}_2$  structures were first created using molecular dynamics (MD) with empirical force fields through a melt-quench procedure. The MD-optimized structures were then re-optimized to the ground state using density functional theory (DFT). MD simulations were performed with the interatomic pair-wise potentials of Kerisit et al.,<sup>36</sup> which are based on the Matsui–Akaogi potentials<sup>37</sup> with the addition of a shell model. The time step for all MD simulations was 2 fs. A Nosé–Hoover thermostat and barostat with time constants of 0.1 and 0.4 ps were used, respectively. Supercells of rutile containing 20,000 atoms were heated at a rate of 117.5 K/ps up to 5000 K and then held at this temperature for 40 ps to ensure

homogeneous mixing. They were then cooled down to room temperature at a rate of 0.235 K/ps for 10 ps in an isothermal–isobaric ensemble (NPT).

DFT calculations were performed using a spin-polarized plane-wave method, as implemented in the Vienna ab initio simulation package.<sup>38,39</sup> The generalized gradient approximation with the Perdew–Burke–Ernzerhof functional was used to approximate the electron exchange and correlation,<sup>40</sup> with a plane-wave kinetic energy cutoff of 500 eV. The projector augmented wave method was used to model the core and valence electronic interactions.<sup>41,42</sup> The electronic configurations of Li, Ti, and O have 3, 4, and 6 valence electrons, respectively. Structural optimizations were performed by allowing the ions and cells (shape and volume) to relax until the energy difference between two consecutive steps was  $<1 \times 10^{-6}$  eV and the Hellman–Feynman forces were less than 0.01 eV/Å. The dispersion forces were considered by applying the DFT-D3 method of Grimme,<sup>43</sup> which is known to improve the structural description of TiO<sub>2</sub><sup>44</sup> and also to improve the structural description of organic solvent molecules in the half-cell electrode system.<sup>44,45</sup>

Lithium-ion insertion was investigated in the crystalline structures of anatase and rutile. The unit cell of anatase TiO<sub>2</sub> has a crystal structure with a space group of *I4<sub>1</sub>/amd* and lattice parameters of  $a = 3.821$  Å and  $c = 9.550$ .<sup>46,47</sup> Rutile TiO<sub>2</sub> has a crystal structure with a space group of *P4<sub>2</sub>/mnm* and lattice parameters of  $a = 4.642$  Å and  $c = 2.961$  Å.<sup>47,48</sup> Rock salt TiO<sub>2</sub> has a crystal structure with a space group of *Fm3m* with a lattice parameter of  $a = 4.840$  Å.<sup>49</sup> Spinel TiO<sub>2</sub> has a crystal structure with a space group of *Fd3m* with a lattice parameter of  $a = 8.339$  Å.<sup>46,49</sup>

Lithiation in the electrodes was modeled in the bulk models using two complementary techniques: random sampling (RS) and site-occupation disorder (SOD). In the RS approach, different numbers of Li atoms were added to the TiO<sub>2</sub> supercells in progressive mole fractions ( $x$ ), occupying randomly selected interstitial sites. Figure S1 (Supporting Information) depicts models of unlithiated and fully lithiated anatase, rutile, and amorphous TiO<sub>2</sub>. For each stoichiometry, the Li <sub>$x$</sub> TiO<sub>2</sub> structure with the lowest energy was chosen as the starting configuration for the calculation of the next Li <sub>$x+\Delta x$</sub> TiO<sub>2</sub> stoichiometry. This was performed in supercells of 24 Ti and 48 O atoms (for amorphous), 36 Ti and 72 O atoms (for anatase  $3 \times 3 \times 1$ ), and 16 Ti and 32 O atoms (for rutile  $2 \times 2 \times 2$ , spinel  $1 \times 1 \times 1$ , and rock salt  $2 \times 2 \times 1$ ) with Monkhorst–Pack  $k$ -point grids of  $3 \times 3 \times 3$  (amorphous),  $3 \times 3 \times 5$  (anatase),  $3 \times 3 \times 5$  (rutile),  $5 \times 5 \times 5$  (spinel), and  $5 \times 5 \times 3$  (rock salt). Following the lithiation of supercells, the evolution of the crystal structure (i.e., atomic coordinates and volume) into different phases was evaluated for each  $x$ . The occurrence of phase transformation following progressive lithiation was investigated here by considering the energy of different TiO<sub>2</sub> polymorphs (i.e., rutile, anatase, rock salt, spinel, and amorphous). Figure 1a–c depicts models of unlithiated and fully lithiated anatase, rutile, and amorphous TiO<sub>2</sub>. In the SOD approach,<sup>50</sup> all possible Li<sup>+</sup> configurations were considered for each  $x$  (see Table S1, Supporting Information), where space group operations were exploited to reduce the configurational space to the symmetry-unique sets. To achieve this, smaller supercells comprising 16 Ti and 32 O atoms (anatase), 8 Ti and 16 O atoms (rutile), and 16 Ti and 32 O atoms (spinel) using  $k$ -point grids of  $2 \times 2 \times 2$  (anatase),  $2 \times 4 \times 3$  (rutile),  $2 \times 2 \times 2$  (spinel) were used. This approach ensured that (a) the lowest energy configuration for each  $x$  was captured and (b) configurational entropy information of the systems is obtained exactly. The drawback of this approach was the limited system size and the associated finite-size effect. Consequently, the larger-supercell RS approach (described above) was also used. In both approaches, the structures were energy-minimized by relaxing the supercell shape and size as well as atomic coordinates. The Bader analysis showed that Li atoms become positively charged at approximately +1 when added into each of the anatase, rutile, and amorphous TiO<sub>2</sub> supercells.

The formation energy of Li <sub>$x$</sub> TiO<sub>2</sub> as a function of  $x$ ,  $U_f(x)$ , was calculated using

$$U_f(x) = U_{\text{Li}_x\text{TiO}_2} - U_{\text{TiO}_2(\text{rutile})} - xU_{\text{Li}} \quad (1)$$

where  $U_{\text{Li}_x\text{TiO}_2}$ ,  $U_{\text{TiO}_2(\text{rutile})}$ , and  $U_{\text{Li}}$  are the DFT energies of Li <sub>$x$</sub> TiO<sub>2</sub>, the TiO<sub>2</sub> functional unit in its rutile structure, and the Li atom in its metal body-centered cubic (bcc) crystal structure, respectively. The Li insertion energy in TiO<sub>2</sub> ( $U_{\text{Li Insertion}}$ ) as a function of  $x$  with a reference to Li metal is given by

$$U_{\text{Li Insertion}} = \frac{U_{\text{Li}_x\text{TiO}_2} - U_{\text{TiO}_2} - xU_{\text{Li}}}{x} \quad (2)$$

where  $U_{\text{TiO}_2}$  is the DFT energy of TiO<sub>2</sub> in the corresponding TiO<sub>2</sub> polymorph structure.

The change of the TiO<sub>2</sub> volume ( $\Delta V$ ) following lithiation was calculated using

$$\Delta V(x) = \frac{V(x) - V_0}{V_0} \times 100\% \quad (3)$$

where  $V(x)$  and  $V_0$  are the volume of Li <sub>$x$</sub> TiO<sub>2</sub> and the volume of TiO<sub>2</sub>, respectively. The configurational average of the volume at temperature  $T$  was calculated using

$$\Delta V = \frac{\sum_i \Delta V(x_i) n(x_i) \exp\left(-\frac{U(x_i)}{k_B T}\right)}{\sum_i n(x_i) \exp\left(-\frac{U(x_i)}{k_B T}\right)} \quad (4)$$

where  $n$  is the number of equivalent configurations and  $k_B$  is the Boltzmann constant.

The modeling of applied potential and charge-transfer reaction during lithiation of a TiO<sub>2</sub> electrode was based on the thermodynamic cycle shown in Figure S4. This cycle includes the migration of Li<sup>+</sup> from the electrolyte to the electrode surface. This was computed using a surface model (a slab) of pristine TiO<sub>2</sub>, as described below. Since the Bader analysis confirmed that inserted Li atoms had an  $\sim +1$  charge (i.e., Li<sup>+</sup>) at all sites extending from the ethylene carbonate (EC) solvent to the bulk TiO<sub>2</sub>, it was assumed that the charge transfer associated with lithiation and de-lithiation occurs concomitantly with the reduction of Ti<sup>4+</sup> to Ti<sup>3+</sup> and oxidation of Ti<sup>3+</sup> to Ti<sup>4+</sup>, respectively. Kerisit et al. reported that a strong binding exists between Li<sup>+</sup> and the electron in TiO<sub>2</sub>,<sup>51</sup> indicating that the migration of Li<sup>+</sup> is always accompanied with the migration of electrons in the electrode.

At electrochemical equilibrium, the rate of lithiation equals the rate of de-lithiation (i.e.,  $\Delta G = 0$ ). Consequently, the equilibrium potential ( $\Delta G = -nFE$ ) for reduction (lithiation) and oxidation (de-lithiation) reactions can be obtained. The Li <sub>$x$</sub> TiO<sub>2</sub> electrode potential ( $E$ ) at equilibrium as a function of  $x$  (vs Li<sup>+</sup>|Li) was calculated using

$$E(x) = -\frac{(U_{\text{Li Insertion}} - U_{\text{Li Vap}} - U_{\text{Li Ion}} - U_{\text{Li Solv}})}{xF} + 1.4 \text{ V} \quad (5)$$

where  $F$  is Faraday's constant and the value of 1.4 V was used to relate the electrode potential from vacuum to the Li<sup>+</sup>|Li standard potential. This value was obtained from the conversion from vacuum to the standard hydrogen electrode (SHE) potential (4.45 V vs vacuum) and from SHE to the standard potential of Li|Li<sup>+</sup> in aqueous electrolytes (3.05 V vs SHE).

To study Li<sup>+</sup> diffusion in the bulk TiO<sub>2</sub>, the migration energy barrier was investigated using the ApproxNEB method<sup>52</sup> using different supercells of 16 Ti and 32 O atoms (amorphous), 36 Ti and 72 O atoms (anatase  $3 \times 3 \times 1$ ), and 24 Ti and 48 O atoms (rutile  $2 \times 2 \times 3$ ). The Monkhorst–Pack  $k$ -point grids of  $3 \times 3 \times 3$  (amorphous),  $3 \times 3 \times 5$  (anatase), and  $3 \times 3 \times 3$  (rutile) were used, respectively. The calculations were performed under constrained lattice parameter conditions (only atomic coordinates were relaxed) since only a single Li atom was added to the supercell. This corresponds to solid-state Li<sup>+</sup> diffusion at  $x = 0.028$  (anatase),  $x = 0.042$  (rutile), and  $x = 0.0625$  (amorphous). The energy barrier for Li<sup>+</sup> migration in bulk anatase and rutile TiO<sub>2</sub> was calculated using both the nudged elastic band (NEB) and ApproxNEB methods (see Figure S6, Supporting Information), and it was found that there was

no significant difference in the energy barrier calculated using the two methods. For amorphous TiO<sub>2</sub>, multiple Li<sup>+</sup> insertion sites were evaluated first and then the energy barrier was calculated for Li<sup>+</sup> migration from one site to another site using ApproxNEB methods. For crystalline TiO<sub>2</sub>, the migration of Li<sup>+</sup> was modeled between stable interstitial sites.

The diffusivity (*D*) of Li<sup>+</sup> in the bulk TiO<sub>2</sub> was calculated using the transition-state theory (TST) method<sup>53</sup> using eqs 6 and 7 with the assumption that the highest energy jump is the rate-limiting jump for bulk Li<sup>+</sup> diffusion

$$D = D_0 \exp\left(-\frac{U_m^b}{k_B T}\right) \quad (6)$$

where *D*<sub>0</sub> is the pre-exponential factor and *U*<sub>m</sub><sup>b</sup> is the migration energy of Li<sup>+</sup> diffusion in bulk TiO<sub>2</sub>. The value of *D*<sub>0</sub> was calculated by taking into account the contributions of the dynamical correction factor (*ξ*), number of equivalent jumps (*g*), jump distance (*l*), attempt frequency (*v*<sup>\*</sup>), and dimensionality of space in which diffusion takes place (*α*)

$$D_0 = \frac{\xi g l^2 v^*}{2\alpha} \quad (7)$$

The value of *ξ* for Li<sup>+</sup> jumps was set to unity, as justified by Kerisit et al.<sup>61</sup> and Milman et al.<sup>51,53</sup> The attempt frequency was calculated using the moving atom approximation<sup>51,54,55</sup> as the product of the three vibrational frequencies (*v*<sub>*i*</sub>) associated with the moving atom at a stable state divided by the product of the two real vibrational frequencies (*v*<sub>*j*</sub>) associated with the moving atom at the transition state according to

$$v^* = \prod_{i=1}^3 v_i / \prod_{j=1}^2 v_j \quad (8)$$

The migration energy (*U*<sub>m</sub>) was obtained by subtracting the DFT energy of the initial state (*U*<sub>IS</sub>) from that of the transition state (*U*<sub>TS</sub>)

$$U_m = U_{TS} - U_{IS} \quad (9)$$

The migration energy for bulk diffusion of Li<sup>+</sup> is identified as *U*<sub>m</sub><sup>b</sup>, whereas *U*<sub>m</sub><sup>i</sup> and *U*<sub>m</sub><sup>e</sup> are used to indicate the interfacial diffusion of Li<sup>+</sup> (as outlined below) for either insertion or extraction, respectively.

Surface calculations were used to investigate the Li<sup>+</sup> insertion and extraction mechanisms from the electrolyte to the electrode, as shown in Figure S2 (Supporting Information). In this study, only Li<sup>+</sup> migration at the interface (between the surface and first layer of TiO<sub>2</sub>) was considered. A solvent comprising EC was used in the slab models since most commercially produced Li-ion batteries use an electrolyte comprising LiPF<sub>6</sub> in EC mixed with other linear carbonates such as dimethyl carbonate (DMC) or ethyl methyl carbonate (EMC). Co-solvent molecules were not included in the simulations because the modeling of solvent mixtures becomes more complex and expensive with DFT.<sup>45</sup> The PF<sub>6</sub><sup>-</sup> anion was also not included in the electrolyte model because (i) LiPF<sub>6</sub> forms either solvent-shared ion pairs or solvent-separated ion pairs<sup>56</sup> and Li<sup>+</sup> inserts into TiO<sub>2</sub> as an isolated cation and (ii) the excess charge of Li<sup>+</sup> when dissolved in EC was compensated by the introduction of electrons in the electrode.

A reduced plane-wave kinetic energy cutoff of 400 eV and a single *k*-point at  $\Gamma$  were used for surface calculations. To model the surface-bulk configuration, the innermost two atomic layers of the slab model were fixed in space, while the outermost atomic layers were relaxed in space. Although crystallographic orientations of different TiO<sub>2</sub> polymorph surfaces are expected to affect the adsorption of Li<sup>+</sup>, this study considered only the migration of Li<sup>+</sup>, which was already adsorbed on the surface, into the first layer and bulk electrode material. Consequently, differences in surface adsorption due to crystal orientation were not included. A thickness of 8 atomic layers was sufficient for the slab models, and the plot of energy convergence versus thickness is presented in the Supporting Information (see Figure S9). In this study, since Li<sup>+</sup> was introduced on the surface, electrons become localized on the neighboring Ti atoms.

The surface model was used to investigate Li<sup>+</sup> migration at the electrolyte/TiO<sub>2</sub> interface along with the provision of electrons due to the applied potential,  $\Delta E$ . The equilibrium potential was obtained assuming a surface comprising pristine TiO<sub>2</sub> (i.e., a perfectly delithiated TiO<sub>2</sub> electrode). Due to the low Li concentration in the surface models (0.014 for anatase and 0.016 for rutile and amorphous), the calculated equilibrium potential represents the onset potential (*E*<sub>onset</sub>) for lithiation and de-lithiation of pristine TiO<sub>2</sub> (i.e., where the current begins to deviate from 0 in a CV measurement).

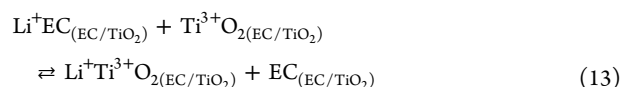
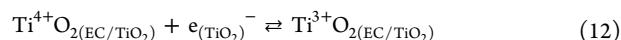
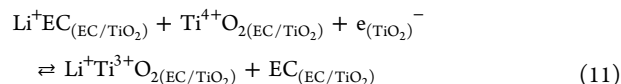
The activation energy as a function of applied potential ( $\Delta E = E - E_{\text{onset}}$ ) for different processes of (i) Li<sup>+</sup> insertion into the surface (*U*<sub>A</sub><sup>i</sup>) and (ii) Li<sup>+</sup> extraction from the surface (*U*<sub>A</sub><sup>e</sup>) is calculated as follows

$$U_A^i(\Delta E) = U_m^i + \beta n F \Delta E \text{ for Li}^+ \text{ insertion (cathodic)} \quad (10a)$$

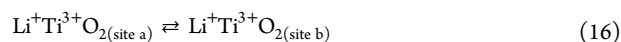
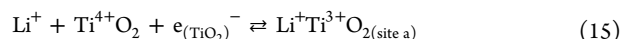
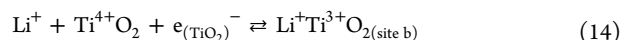
$$U_A^e(\Delta E) = U_m^e - \beta n F \Delta E \text{ for Li}^+ \text{ extraction (anodic)} \quad (10b)$$

where *U*<sub>m</sub><sup>i</sup> and *U*<sub>m</sub><sup>e</sup> are the migration energies for Li<sup>+</sup> insertion (*U*<sub>m</sub><sup>i</sup>) and extraction (*U*<sub>m</sub><sup>e</sup>), which were used to approximate the activation energies at  $\Delta E = 0$  (*U*<sub>A</sub><sup>i</sup>(0) and *U*<sub>A</sub><sup>e</sup>(0)), respectively, and  $\beta$  is the transfer coefficient, which was assumed to be 0.5.<sup>57</sup>

The step reactions that occur during lithiation and de-lithiation of TiO<sub>2</sub> can be categorized into interfacial reaction (eqs 10b–12) and bulk reaction (eqs 13–15). The Li<sup>+</sup>Ti<sup>3+</sup>O<sub>2</sub> (site a) and Li<sup>+</sup>Ti<sup>3+</sup>O<sub>2</sub> (site b) species correspond to systems comprising TiO<sub>2</sub> and a Li<sup>+</sup> atom, where the Li<sup>+</sup> atom is accommodated in one of the two sites which are symmetrically equivalent in anatase and rutile but distinct in amorphous TiO<sub>2</sub>. The reactions at the electrolyte/TiO<sub>2</sub> interface (reaction 11) and in the bulk TiO<sub>2</sub> (reaction 14) can be separated into electron transfer (reactions 12 and 15) and Li<sup>+</sup> migration (reactions 13 and 16). The surface process consists of



while the bulk process consists of



It is important to emphasize that the modeling of Li<sup>+</sup> migrations at the interface and in the bulk performed in this study was assumed to occur at the early stage of lithiation in which small *x* is present in TiO<sub>2</sub>. The extrapolation of *U*<sub>m</sub> for bulk Li diffusion to higher *x* is only valid when Li<sup>+</sup> ions are evenly distributed in a homogeneous Li<sub>*x*</sub>TiO<sub>2</sub>. In other words, the effects of phase transitions were not considered. In practice, such conditions only occur in the early stage of lithiation.

### 3. RESULTS AND DISCUSSION

**3.1. Development of the Amorphous TiO<sub>2</sub> Model.** The developed amorphous TiO<sub>2</sub> structures were validated against experimental radial distribution functions, *g*(*r*). Figure 1a shows the *g*(*r*) comparison between the MD and DFT amorphous TiO<sub>2</sub> models and the distribution determined by Petkov et al. using X-ray diffraction (XRD) analysis of sol-gel and powder amorphous TiO<sub>2</sub>.<sup>58</sup> MD provides a reasonably accurate first approximation of the amorphous TiO<sub>2</sub> structures when compared to the XRD results. Further structural optimization of smaller supercells using DFT was found to

improve the agreement with the experimental  $g(r)$ , especially at  $r > 2.7$  Å. Amorphous  $\text{TiO}_2$  has a density of  $4.34 \text{ g cm}^{-3}$ , suggesting that the amorphous structures are denser than anatase and rutile  $\text{TiO}_2$  ( $3.80$  and  $4.16 \text{ g cm}^{-3}$ , respectively). The densities of crystalline  $\text{TiO}_2$  obtained here are consistent with the previous study by Matsui et al.<sup>37</sup>

Figure 1b shows the  $g(r)$  of amorphous  $\text{TiO}_2$  structures calculated using DFT in different sizes of the supercell and the numbers of atoms. A total of 3 different supercell sizes were modeled with 48 atoms (12 Ti and 36 O), 72 atoms (24 Ti and 48 O), and 108 atoms (36 Ti and 72 O). For each supercell size, at least three different amorphous structures were constructed from the equilibrated structures obtained using the MD simulations. The correlations of Ti–O, O–O, and Ti–Ti atoms were consistent for all supercell sizes. The individual correlations between each chemical species pair are shown clearly in Figure 1c. The first peak in  $g(r)$ , corresponding to the Ti–O correlation, is at a radius of  $\sim 2.0$  Å. However, the second peak in  $g(r)$  at a radius of  $\sim 2.5$  Å corresponds to the O–O correlation. The correlations of Ti–Ti were observed in  $g(r)$  at a radius of  $\sim 3.1$  Å. The peak in the  $g(r)$  observed at  $\sim 3.6$  Å appears to be due to the contributions from the different chemical species pairs of Ti–O, O–O, and Ti–Ti. Two peaks corresponding to the Ti–Ti correlation were observed in anatase and rutile  $\text{TiO}_2$ , with the shorter and longer Ti–Ti correlations being at 3.05 and 3.79 Å for anatase and at 2.96 and 3.66 Å for rutile, respectively.

### 3.2. Thermodynamic Properties of Lithiated $\text{TiO}_2$ .

Lithium ions occupy well-defined sites in the structures of crystalline  $\text{TiO}_2$  polymorphs, implying that a perfect crystalline  $\text{TiO}_2$  material has a theoretical maximum  $\text{Li}^+$  storage of  $x = 1$  for anatase and  $x = 2$  for rutile. In dilute  $\text{Li}^+$  concentrations, anatase  $\text{TiO}_2$  has a stable  $\text{Li}^+$  insertion site at Wyckoff position 4b ( $U_{\text{Li Insertion}} = -2.347 \text{ eV}$ ) and a metastable site at 8d ( $U_{\text{Li Insertion}} = -1.837 \text{ eV}$ ), while rutile  $\text{TiO}_2$  has a stable  $\text{Li}^+$  insertion site at Wyckoff position 4c ( $U_{\text{Li Insertion}} = -1.950 \text{ eV}$ ) and metastable sites at 4d ( $U_{\text{Li Insertion}} = -1.946 \text{ eV}$ ) and 4g ( $U_{\text{Li Insertion}} = 0.063 \text{ eV}$ ). These  $\text{Li}^+$  insertion sites found in anatase and rutile  $\text{TiO}_2$  were in agreement with previous studies.<sup>59,60</sup> In rock salt  $\text{TiO}_2$ ,  $\text{Li}^+$  can occupy Wyckoff position 4b, while in spinel  $\text{TiO}_2$ , the ions can occupy the 8a sites up to concentrations of  $x \leq 0.5$  and the 16c sites at  $0.5 \leq x \leq 1$ . In the dilute limit, the  $U_{\text{Li Insertion}}$  is  $-1.368 \text{ eV}$  in rock salt and  $-4.179 \text{ eV}$  in spinel. Meanwhile, in amorphous  $\text{TiO}_2$ ,  $\text{Li}^+$  can fill any unoccupied free space that can accommodate the volume of  $\text{Li}^+$ .

Since the stable  $\text{Li}^+$  insertion sites have been identified, the investigation of  $\text{Li}_x\text{TiO}_2$  polymorph stability as a function of  $x$  was performed considering multiple possible configurations of  $\text{Li}^+$  in the supercell using both the RS and SOD approaches. In the SOD approach, all 805, 1655, 16, and 417 possible  $\text{Li}^+$  configurations were considered for anatase, rutile, spinel, and rock salt structures, respectively.

Figure 2 shows that the two approaches yield consistent  $U_f$  values. Spinel has relatively higher  $U_f$  than anatase, rutile, and amorphous  $\text{TiO}_2$  at  $x = 0$ ; however, progressive lithiation alters the  $U_f$  significantly. It is revealed that lithiated spinel has a lower  $U_f$  than both lithiated rutile and lithiated anatase at  $x = 0.3$ . Lithiated amorphous  $\text{TiO}_2$  consistently has higher  $U_f$  than lithiated anatase and rutile  $\text{TiO}_2$ . The rock salt ( $Fm\bar{3}m$ )  $\text{TiO}_2$  phase was found to be thermodynamically unstable at all  $x$ , exhibiting higher  $U_f$  than all other phases including amorphous  $\text{TiO}_2$ . Based on the  $U_f$  of different  $\text{TiO}_2$  polymorphs, from the

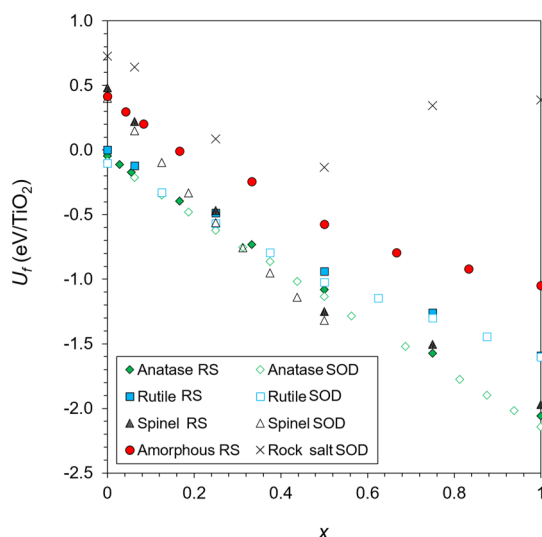
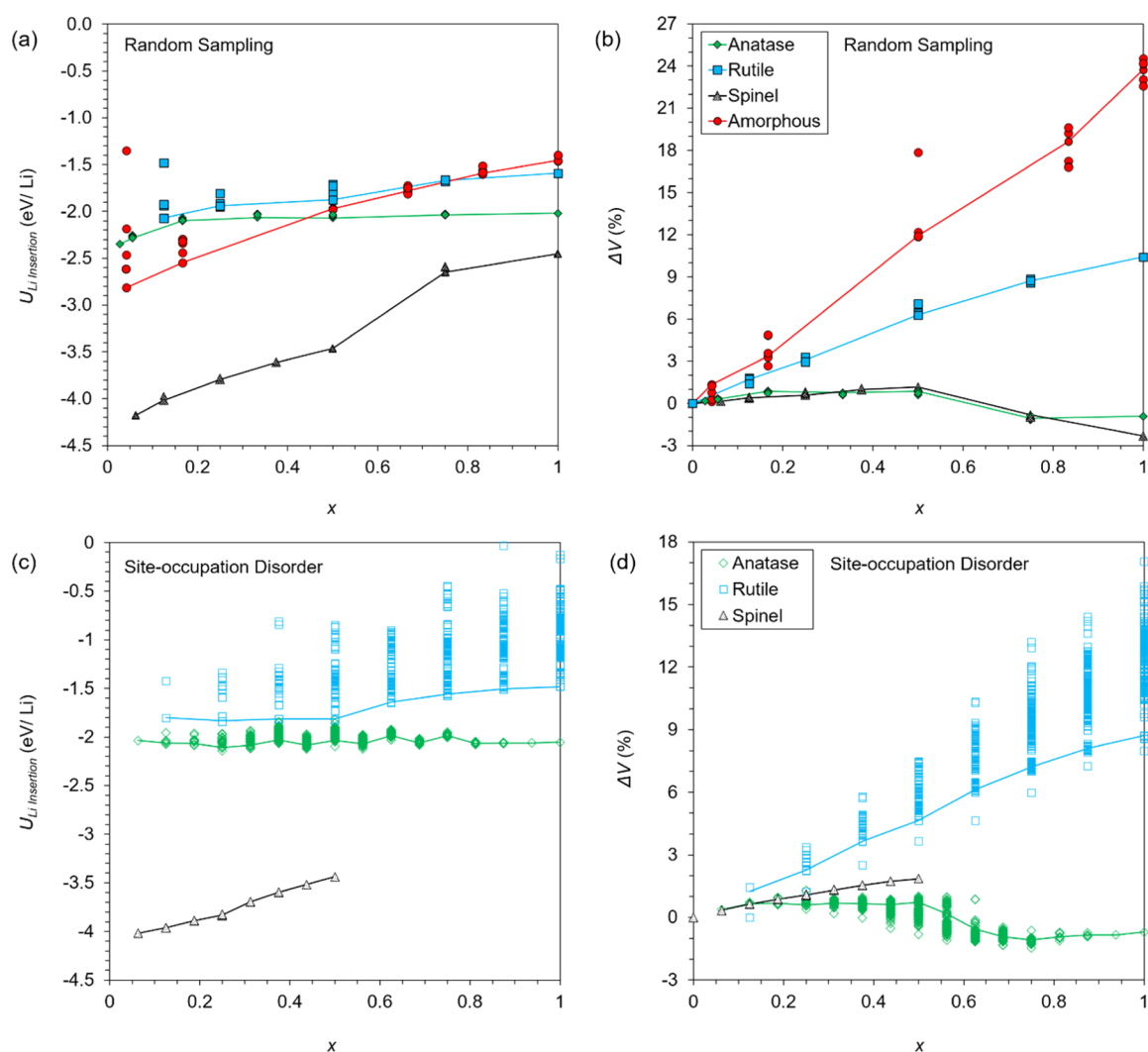


Figure 2. Formation energy ( $U_f$ ) of  $\text{TiO}_2$  polymorphs (anatase, rutile, spinel, amorphous, and rock salt) as a function of  $x$  as calculated using the RS and SOD approaches.

most stable to the least, the order is at  $x = 0$ , anatase > rutile > amorphous > spinel > rock salt; at  $x = 0.5$ , spinel > anatase > rutile > amorphous > rock salt; and at  $x = 1$ , anatase > spinel > rutile > amorphous > rock salt. It is important to note that practically, it is difficult to have a pristine spinel  $\text{TiO}_2$  structure,<sup>36</sup> and in previous experimental studies, the spinel structure was commonly obtained following the lithiation of either anatase<sup>46</sup> or rutile  $\text{TiO}_2$ .<sup>49</sup> Moreover, the changes of the amorphous  $\text{TiO}_2$  structure to the crystalline phase following lithiation is possible at any  $x$  only if the energy barrier for phase transformations is fulfilled, considering that the energy of lithiated amorphous  $\text{TiO}_2$  is much higher than that of lithiated crystalline  $\text{TiO}_2$  (anatase, spinel, and rutile as shown in Figure 2). The  $\text{Li}_x\text{TiO}_2$  stoichiometry has been reported by Xiong et al. to influence the occurrence of phase transformation from amorphous to cubic.<sup>61</sup> They revealed that at low  $x$ , the diffusion of Ti and O atoms is very slow; therefore, the disordered structure is expected to persist. However, at high  $x$ , the diffusion of Ti and O atoms is accelerated so that the formation of the crystalline cubic structure (i.e., short-range ordering) becomes possible.<sup>61–63</sup>

Using the results from the RS and SOD approaches, the  $U_{\text{Li Insertion}}$  for anatase, rutile, spinel, and amorphous  $\text{TiO}_2$  are shown in Figure 3a,c with their corresponding  $\Delta V$  as a function of  $x$ . The  $U_{\text{Li Insertion}}$  calculated using eq 2 increases with increasing  $x$ . Amorphous  $\text{TiO}_2$  has a lower  $U_{\text{Li Insertion}}$  than either anatase or rutile  $\text{TiO}_2$  at  $x < 0.50$ . This suggests that  $\text{Li}^+$  inserts more easily into amorphous  $\text{TiO}_2$  than anatase and rutile  $\text{TiO}_2$  in the early stage of lithiation. The volume change,  $\Delta V$ , of  $\text{Li}_x\text{TiO}_2$  with progressive lithiation is shown in Figure 3b,d. From the RS results, the  $\Delta V$  values at full lithiation (i.e.,  $x = 1$ ) were  $-0.9\%$  (anatase),  $10.4\%$  (rutile),  $-2.3\%$  (spinel), and  $23.7\%$  (amorphous). Where multiple structures were obtained for a given  $x$ ,  $\Delta V$  was calculated as a configurational average at  $T = 300 \text{ K}$ . The occurrence of a structural evolution during lithiation of anatase  $\text{TiO}_2$  contributes to its relatively low, and mostly negative, volume expansion. Lithiation of rutile up to  $x = 1$  causes the volume to expand, and the lowest energy structure results in the smallest volume expansion. Lithiated amorphous  $\text{TiO}_2$  structures exhibit the largest  $\Delta V$  of



**Figure 3.**  $U_{\text{Li Insertion}}$  (a,c) and  $\Delta V$  (b,d) of anatase, rutile, spinel, and amorphous  $\text{Li}_x\text{TiO}_2$  as a function of  $x$  calculated using RS (a,b) and SOD (c,d). The RS results include four anatase (open diamonds), four rutile (open squares), three spinel (solid triangles), and five amorphous (solid circles)  $\text{TiO}_2$  structures. The lines represent the configurational average at  $T = 300$  K for all  $\text{TiO}_2$  polymorphs.

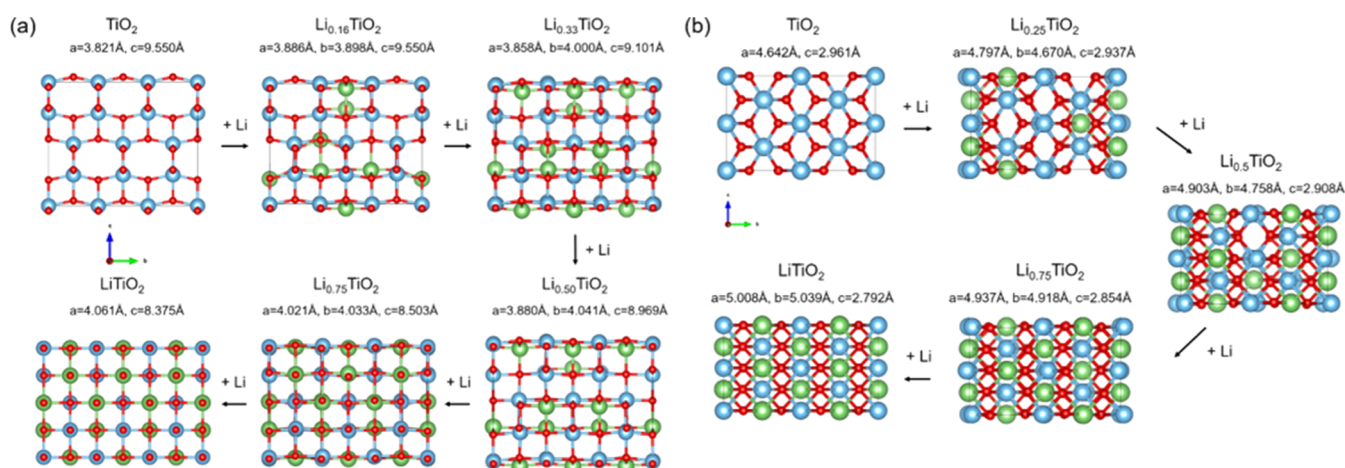


**Figure 4.** Changes in the lowest-energy crystal structures of (a) anatase and (b) rutile with increasing  $\text{Li}^+$  mole fractions ( $0 \leq x \leq 1$ ). For anatase, the crystal structure transforms from  $I4_1/amd$  to  $Imma$  and back to  $I4_1/amd$  with progressive lithiation. For rutile, progressive lithiation results in a crystal structure transformation from  $P4_2/mnm$  to  $P2_1/m$ .

23.7%. This has implications for structural changes in the electrodes if such high lithiation mole fractions are attempted.

The structural evolution pathways for anatase and rutile are shown in Figure 4. These pathways are in agreement with

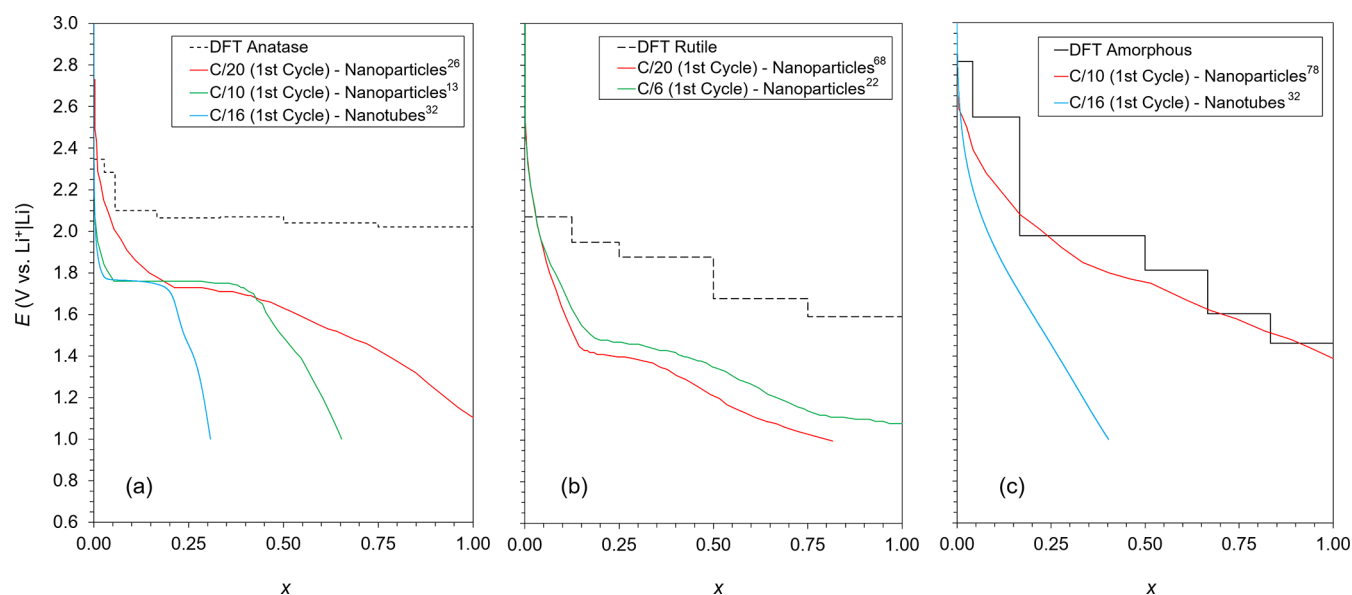


**Figure 5.** Potential of bulk  $\text{Li}_x\text{TiO}_2$  electrodes calculated using eq 5 for (a) anatase ( $I4_1/amd \rightarrow Imma \rightarrow I4_1/amd$ ), (b) rutile ( $P4_2/mnm \rightarrow P_2/m$ ), and (c) amorphous as a function of  $x$ . The black lines represent the DFT-calculated potentials with the lowest energy configurations and red, green, and blue lines represent the experimentally recorded potentials for  $\text{Li}_x\text{TiO}_2$  electrodes.

previous DFT investigations.<sup>64,65</sup> Progressive lithiation of anatase and rutile  $\text{TiO}_2$  was found to result in a slight evolution of the crystal structure, involving the shuffling of Ti and O atoms.

Anatase underwent a structural evolution forming an *Imma* crystal phase at  $x > 0.16$  and then forming an  $I4_1/amd$  phase at  $x > 0.75$ . These two phases, *Imma* and  $I4_1/amd$ , differ solely in the angle of the Ti–O–Ti bonds and the associated volume reduction. The most thermodynamically favorable phase for fully lithiated anatase  $\text{TiO}_2$  is  $I4_1/amd$ , which has been experimentally reported as  $\gamma\text{-LiTiO}_2$ .<sup>66</sup> The volume change in anatase  $\text{TiO}_2$  from  $I4_1/amd$  to *Imma* is caused by the shortening of the *c*-axis and lengthening of the *a*-axis. At low  $x$ , the lengthening effect of *a*-axis is dominant and leads to a volume increase in anatase with lithiation. This is in agreement with the experimental observation of less than 4% volume expansion in anatase with the low  $\text{Li}^+$  mole fraction.<sup>64</sup> Increasing  $\text{Li}^+$  mole fraction further induces the structural evolution described above, which causes a reduction in volume due to the shortening of the *c*-axis dominating over the lengthening of the *a*-axis. Additionally, Cava et al. reported a transformation of  $\text{Li}_{0.5}\text{TiO}_2$  from lithiated anatase (*Imma*) to  $\text{LiTi}_2\text{O}_4$  spinel (*Fd3m*) at high temperatures and attributed it to extensive crystallographic strain relief.<sup>46</sup> This transformation is also found to be thermodynamically feasible from the calculated values of  $U_f$  (see Figure 2).

Rutile also underwent a structural evolution to the  $P_2/m$  crystal at  $x \geq 0.25$  with a constant increase of  $U_{\text{Li Insertion}}$  with lithiation up to  $x = 1$ . Among all the phases, spinel *Fd3m* exhibits remarkably low  $U_{\text{Li Insertion}}$ , suggesting that the lithiation reaction is more likely to be irreversible. The  $U_{\text{Li Insertion}}$  increases significantly at  $x > 0.5$ , when  $\text{Li}^+$  starts to occupy  $16c$  sites and the increasing Li–Li repulsion becomes more evident in the structure. Further lithiation at  $x > 1$  is believed to be no longer practically possible in crystalline electrodes due to i) unavailability of  $\text{TiO}_2$  redox centers ( $\text{Ti}^{4+} \rightleftharpoons \text{Ti}^{3+}$ ) and  $\text{Li}^+$  insertion sites, ii) increasing Li–Li repulsion forces, and iii) limited diffusivity of  $\text{Li}^+$  in the structure. For

rutile  $\text{TiO}_2$ , the insertion of  $\text{Li}^+$  at  $x > 1$  leads to a significant increase in  $U_{\text{Li Insertion}}$  from  $-1.592$  (at  $x = 1$ ) to  $-1.070$  eV (at  $x = 1.25$ ) if it maintains its  $P_2/m$  crystal and thus possibly transforms into an irreversible phase of  $P_2/m_{\text{HEX}}$ , which is a layered monoclinic structure.<sup>65,67</sup>

The results from the RS approach show that rutile  $\text{LiTiO}_2$  exhibits a moderate volume expansion of 10.4% with a single-phase transformation from  $P4_2/mnm$  to  $P_2/m$ . The most stable  $\text{LiTiO}_2$  structure was obtained when Li atoms were far apart with an atomic (Li–Li) separation of 2.79 Å. The irreversible capacity observed in rutile  $\text{TiO}_2$ ,<sup>48,68</sup> which has been associated previously with the formation of an SEI film on the surface,<sup>69,70</sup> may be explained more appropriately by the occurrence of this phase transformation. Borghols et al. reported that rutile  $\text{TiO}_2$  transforms from an unlithiated  $P4_2/mnm$  to a lithiated  $P_2/m$  crystal,<sup>65</sup> however, transformation of rutile to other phases, such as *Fd3m* and *Fm3m*, has also been reported.<sup>49,71</sup> Rutile  $P4_2/mnm$  may transform into a *Fd3m* crystal (spinel) following lithiation (as proposed by Vijayakumar et al.<sup>49</sup>) since spinel has a lower  $U_f$  than rutile at  $x > 0.25$ . This transformation is evident from the observation of an additional XRD peak and a plateau region in galvanostatic charge–discharge measurements in lithiated rutile.<sup>49</sup> Alternatively, rutile may also follow the anatase transformation via  $I4_1/amd$  and *Imma* crystals<sup>36</sup> since anatase has lower  $U_f$  than rutile at  $x \geq 0$ . On the other hand, it is unlikely that lithiation of the  $P4_2/mnm$  crystal results in a transformation into a *Fm3m* (rock salt) crystal phase, as reported by Baudrin et al.,<sup>71</sup> since rock salt was found to have a higher  $U_f$  than rutile at any  $x$ .

In amorphous  $\text{TiO}_2$ , Li ions can occupy any sites in the structure, and consequently, the maximum  $\text{Li}^+$  storage can theoretically exceed  $x > 1$ . However, further lithiation is no longer thermodynamically favored due to the unavailability of associated  $\text{TiO}_2$  redox centers. A wide range of  $U_{\text{Li Insertion}}$  values was observed and is shown in Figure 3a since amorphous  $\text{TiO}_2$  has numerous non-equivalent  $\text{Li}^+$  insertion sites, especially at low  $x$ . Increasing  $x$  in amorphous  $\text{TiO}_2$

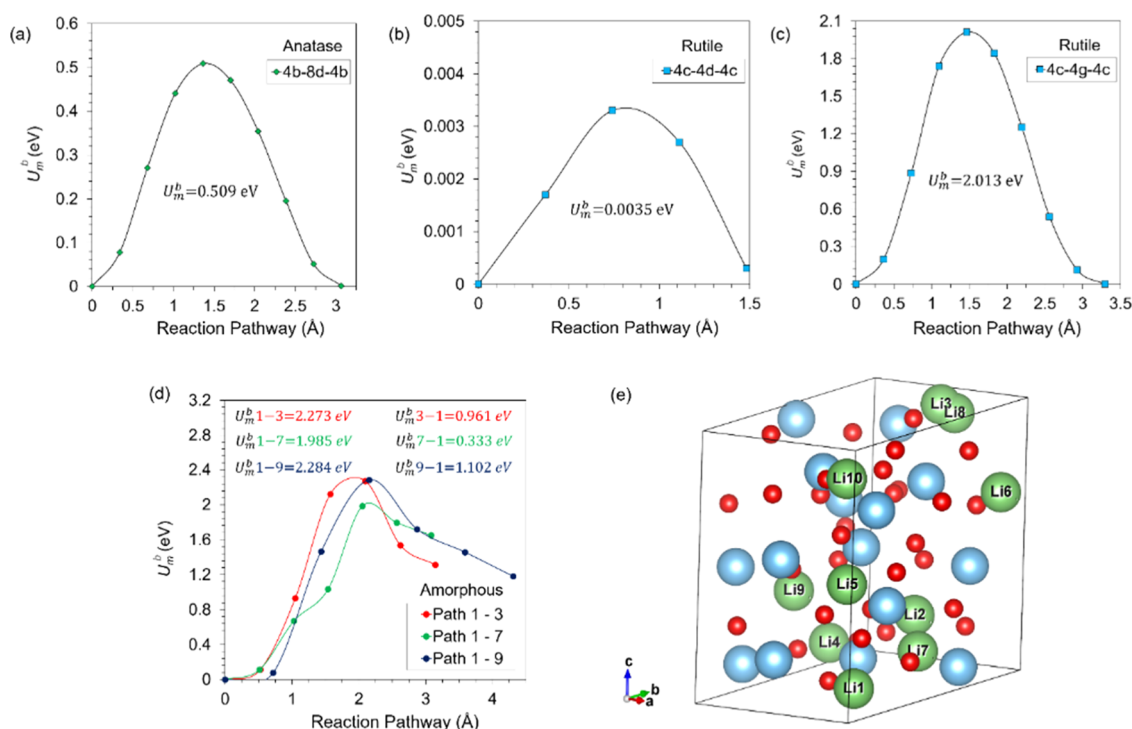


**Figure 6.**  $U_m^b$  for the minimum energy pathway of  $\text{Li}^+$  migration in the bulk anatase (a) and rutile  $\text{TiO}_2$  (b,c). (d)  $U_m^b$  for three minimum energy pathways of  $\text{Li}^+$  migration in bulk amorphous  $\text{TiO}_2$  from different possible  $\text{Li}^+$  insertion sites considered as in (e). Red, blue, and green balls represent O, Ti, and Li atoms, respectively.

necessarily causes shorter chemical pairs (i.e., Li–O, Li–Ti, and Li–Li) in the structures. This in turn is believed to lead to the increase of  $U_{\text{Li Insertion}}$  and the reduction of its variability at each  $x$ , similar to the principle proposed by Arrouvel et al.,<sup>72</sup> who suggested that the lowest energy for  $\text{Li}^+$  insertion in a  $\text{TiO}_2$  polymorph was achieved when the distance between Li and Ti atoms is maximized. In the current work, the most energetically favorable lithiation site at low  $x$  was identified when the Li atom is separated at maximum distances from its neighboring Ti and O atoms (see Figure S7, Supporting Information). The large volume expansion predicted here has not been reported in the experiments, and this may correspond to (i) a poor packing density of amorphous  $\text{TiO}_2$  electrodes in experiments, (ii) a lower  $\text{Li}^+$  mole fraction achieved in experiments,<sup>73,74</sup> and/or (iii) changes in the kinetics due to progressive lithiation.<sup>62,63,75</sup> In other words, although full lithiation may not be thermodynamically limited for amorphous  $\text{TiO}_2$ , the negative impacts of the resulting large  $\Delta V$  would be expected to introduce durability issues that would limit the electrode cycle life.

**3.3. Electrochemical Properties of Lithiated  $\text{TiO}_2$ .** The equilibrium potentials of bulk anatase, rutile, and amorphous  $\text{TiO}_2$  electrodes were calculated using eq 5. The results are presented in Figure 5 and compared with the electrode potentials obtained from previously reported experiments. The equilibrium potential for spinel  $\text{TiO}_2$  was not considered here since spinel is not present in pristine  $\text{TiO}_2$ . The  $E_{\text{onset}}$  obtained from the thermodynamic cycle in Figure S4 was calculated as 2.13 V (anatase) and 1.85 V (rutile). For amorphous  $\text{TiO}_2$ , the  $E_{\text{onset}}$  were found to be in the range of 1.13–2.60 V. The lithiation and de-lithiation peaks for amorphous  $\text{TiO}_2$  do not converge to a single value and are consequently shown as a broad peak due to the absence of well-defined equivalent sites on the surface for  $\text{Li}^+$  insertion.

The DFT-calculated potentials as a function of  $x$  are represented by step changes due to the discrete calculations of  $\text{Li}_x\text{TiO}_2$  potential and for anatase and rutile include the structural evolution described in Figure 4. Anatase and rutile  $\text{TiO}_2$  exhibit three potential regions, with a plateau region being found at  $x = 0.0625$  to 1.0 for anatase and at  $x = 0.125$  to 0.50 for rutile. In contrast, a continuously decreasing potential with lithiation is observed for amorphous  $\text{TiO}_2$ . Anatase, rutile, and amorphous  $\text{TiO}_2$  can effectively accommodate  $\text{Li}^+$  in the structures up to  $x = 1.0$ , indicating full lithiation.

Anatase  $\text{TiO}_2$  exhibits a plateau in its lithiation potential, which corresponds to the occurrence of the structural evolution of  $I4_1/amd \rightarrow Imma \rightarrow I4_1/amd$  crystal structures with increasing  $x$ . Delaying the phase transformation to the  $Imma$  crystal structure can be achieved by using nano-sized crystallites, which allow higher  $\text{Li}^+$  mole fractions to be inserted in the electrode.<sup>26</sup> This recorded higher capacity can be explained from a decreasing contribution of  $\text{Li}^+$  bulk storage and an increasing contribution of  $\text{Li}^+$  surface storage in the nano-sized electrodes. Adding  $\text{Li}^+$  into a rutile  $\text{TiO}_2$   $P4_2/mnm$  crystal leads to the formation of the  $P_2/m$  phase in a fully lithiated state. No plateau region is observed in the lithiation of rutile  $\text{TiO}_2$  via  $P4_2/mnm \rightarrow P_2/m$ , suggesting a solid-solution  $\text{Li}^+$  insertion mechanism. The maximum capacity in rutile is marked by a significant potential drop from 1.43 V at  $x = 1$  to 0.83 V at  $x = 1.25$  due to the increasing Li–Li repulsion in the structure.

In the case of amorphous  $\text{TiO}_2$ , the potential decreases linearly with increasing  $x$ . There is no observation of amorphous-to-cubic phase transformation during lithiation as proposed previously by Xiong et al.,<sup>61</sup> suggesting that  $\text{Li}^+$  capacity at  $x \leq 1$  is accommodated in the flexible structure of amorphous  $\text{TiO}_2$ . It is possible that the amorphous-to-cubic transformation reported by Xiong et al. starts to occur at  $x > 1$

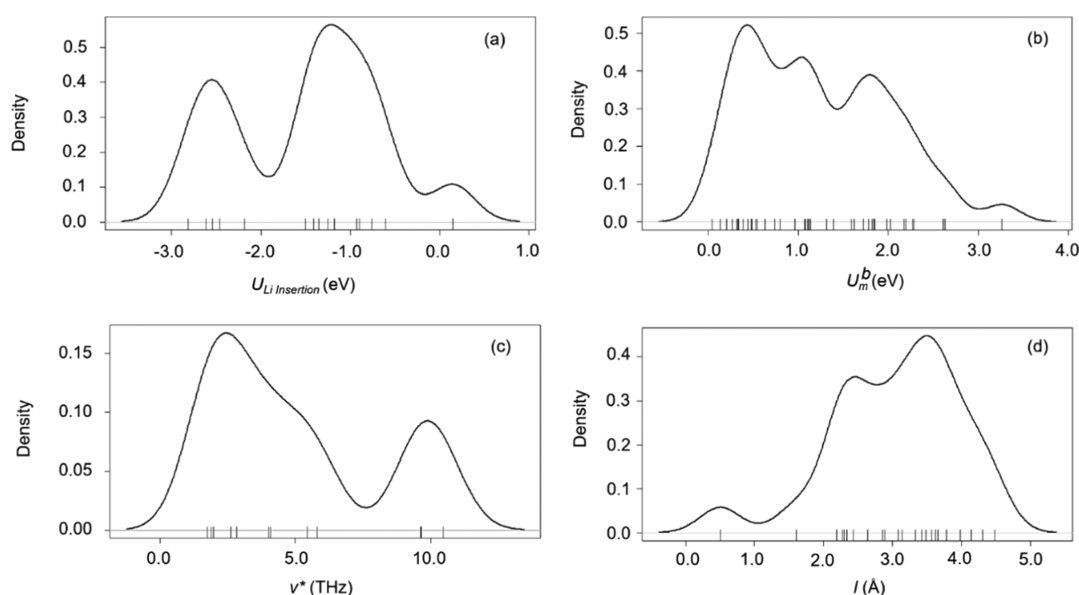


**Figure 7.** Density plots of (a)  $U_{Li\ Insertion}$ , (b)  $U_m^b$ , (c)  $\nu^*$ , and (d)  $l$  in amorphous TiO<sub>2</sub> structures. The dashes at the bottom of each graph represent the individual DFT-calculated values.

(see Figure 5c). Phase transitions from amorphous to cubic may occur at the surface, where the concentration of Li<sup>+</sup> is the highest.<sup>62,63</sup> The occurrence of this transformation is expected to depend on competing thermodynamic and kinetic factors, considering that increasing  $x$  also leads to increases in the Ti and O diffusivities.<sup>61–63</sup>

Overall, the DFT-calculated equilibrium potentials are consistent with the experimentally recorded potentials, as shown from the slope changes following lithiation. Comparisons between calculated and experimentally measured Li<sub>*x*</sub>TiO<sub>2</sub> electrodes are best made from the lithiation of pristine TiO<sub>2</sub> to avoid the contributions of irreversibly inserted Li<sup>+</sup> from prior charging cycles. Experimental reports are not always clear on whether any prior pre-lithiation has been performed; however, in this study, comparisons were made with data from the first cycle lithiation of pristine TiO<sub>2</sub> electrodes (see Figure 5).

**3.3.1. Diffusion of Li<sup>+</sup> in Bulk TiO<sub>2</sub>.** The present investigations aimed to provide kinetic insights into the lithiation and de-lithiation processes for anatase, rutile, and amorphous TiO<sub>2</sub> by calculating the energy barrier ( $U_m^b$ ) for Li<sup>+</sup> migration in the bulk structures. Anatase TiO<sub>2</sub> has only one stable interstitial site for Li<sup>+</sup> insertion (4b) and one Li<sup>+</sup> jump via the 8d site. Lithium diffusion in bulk anatase TiO<sub>2</sub> is found to be isotropic and follows a zigzag path with a jump length of 3.065 Å. The  $U_m^b$  for dilute Li<sup>+</sup> diffusion in anatase is 0.509 eV, as shown in Figure 6a, with  $\nu^* = 6.653$  THz. For Li<sup>+</sup> diffusion in anatase, the values of  $g = 4$ ,  $l = 3.065$ , and  $\alpha = 3$  were used to calculate  $D$  analytically, resulting in a diffusivity of  $4.167 \times 10^{-3} \exp(-0.509 \text{ eV}/k_B T) \text{ cm}^2 \text{ s}^{-1}$ .

Rutile TiO<sub>2</sub> also has only one stable Li<sup>+</sup> insertion site (4c), but there are two possible Li<sup>+</sup> jumps, which occur via the 4d and 4g sites. As a result, the diffusion of Li<sup>+</sup> in bulk rutile TiO<sub>2</sub> is anisotropic, with *c*-axis migration (following path 4c–4d–4c, see Figure 6b) exhibiting a very small  $U_m^b$  of 0.004 eV, and basal migration (following path 4c–4g–4c, see Figure 6c) has higher  $U_m^b$  of 2.013 eV. The pre-exponential factors were calculated using  $g = 2$ ,  $l = 1.483$  Å,  $\alpha = 1$ , and  $\nu^* = 5.68$  THz for *c*-axis migration and  $g = 4$ ,  $l = 3.294$  Å,  $\alpha = 2$ , and  $\nu^* = 2.44$  THz for basal migration. The resulting diffusivities were  $8.331$

$\times 10^{-4} \exp(-0.004 \text{ eV}/k_B T) \text{ cm}^2 \text{ s}^{-1}$  for *c*-axis diffusion and  $1.766 \times 10^{-3} \exp(-2.013 \text{ eV}/k_B T) \text{ cm}^2 \text{ s}^{-1}$  for basal diffusion.

The energy barrier for Li<sup>+</sup> diffusion via the *c*-axis in rutile is extremely low, and this is due to the use of a large supercell which is able to accommodate lattice strain in the structure and minimize Li–Li interactions in the supercell. Previous studies,<sup>51,59,76,77</sup> which used a smaller supercell, reported a higher value of  $U_m^b$  for *c*-axis migration in rutile of 0.040 eV. A similar value of 0.036 eV was reproduced when repeating the calculations in a unit cell. This confirms that this jump is strongly sensitive to finite size effects and suggests that a large supercell must be used to calculate dilute Li<sup>+</sup> diffusion in rutile. Even at high Li<sup>+</sup> concentrations, the use of a unit cell is inappropriate as it simulates the concerted motion of all Li atoms, which is a not a realistic representation of Li<sup>+</sup> diffusion in rutile.

For amorphous TiO<sub>2</sub>, the calculations of  $U_m^b$  become more complicated as there are no well-defined sites for Li<sup>+</sup> insertion. Therefore, ten possible sites in amorphous TiO<sub>2</sub> structures were identified (see Figure 6e), and from these sites, several possible jumps were evaluated. The minimum energy path of selected Li<sup>+</sup> jumps (both the forward and backward) is shown in Figure 6d, and details of the individual jumps are reported in Table S3 in the Supporting Information. It is important to understand that there are numerous sites available for Li<sup>+</sup> insertion in amorphous TiO<sub>2</sub> for  $x = 0.0625$ , as illustrated in a density plot of  $U_{Li\ Insertion}$  in Figure 7. The value of  $U_{Li\ Insertion}$  ranges between  $-2.815$  and  $0.152$  eV, with the highest frequency of occurrence at  $-1.14$  eV. The  $U_m^b$  for Li<sup>+</sup> diffusion in amorphous TiO<sub>2</sub> ranges from 0.04 to 3.26 eV, and the  $\nu^*$  ranges from 1.75 to 10.45 THz. The highest frequency of occurrence of  $U_m^b$ ,  $\nu^*$ , and the jump length are found at 0.60 eV, 3.05 THz, and 3.415 Å, respectively. The estimated range of  $U_m^b$  encompasses the range of 0.305–0.697 eV calculated by Yildirim et al. using MD with the shell potential model<sup>75</sup> and the lower value of 0.16 eV estimated using NMR by Borghols et al.<sup>78</sup> It is particularly difficult to calculate the diffusion coefficient of Li<sup>+</sup> in amorphous TiO<sub>2</sub> using DFT as there are

practically an infinite number of possible  $\text{Li}^+$  diffusion paths and all paths could not be considered in this study.

The correlation between  $U_{\text{Li Insertion}}$  (at the initial site) and  $U_{\text{m}}^{\text{b}}$  for amorphous  $\text{TiO}_2$  is shown in Figure 8, together with

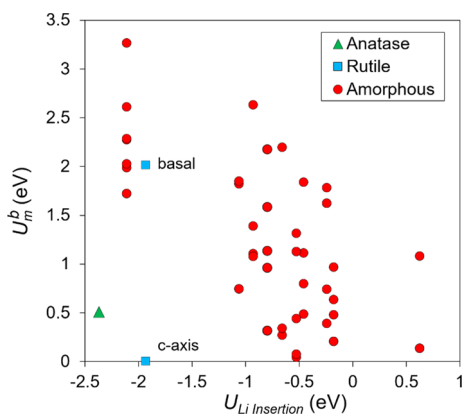


**Figure 8.** Correlation between values of  $U_{\text{m}}^{\text{b}}$  and  $U_{\text{Li Insertion}}$  at initial state for  $\text{Li}^+$  ion diffusion in anatase, rutile, and amorphous  $\text{TiO}_2$ .

the values for anatase and rutile for comparison. It is important to note that these values are for dilute  $\text{Li}^+$  concentrations. The accumulation of  $\text{Li}^+$  in the structure beyond the dilute limit is believed to alter this trend due to increasing Li–Li repulsion forces. In anatase and rutile, both  $U_{\text{Li Insertion}}$  and  $U_{\text{m}}^{\text{b}}$  are low in the dilute limit. In contrast, a strong anti-correlation is observed in amorphous  $\text{TiO}_2$  between the insertion energy and migration energy of  $\text{Li}^+$ . When  $\text{Li}^+$  occupies low energy sites, it requires a significantly higher  $U_{\text{m}}^{\text{b}}$  to jump to another site than when it occupies higher energy sites. This suggests that the flexibility of the amorphous  $\text{TiO}_2$  structure can facilitate the diffusion of  $\text{Li}^+$  even at a high  $x$ , knowing that the most energetically favourable  $\text{Li}^+$  insertion sites are achieved when the Li–O, Li–Ti, and Li–Li atom pairs have their largest separation. In addition, concerning the relation between  $U_{\text{Li Insertion}}$  and  $U_{\text{m}}^{\text{b}}$  in amorphous  $\text{TiO}_2$ , it can be proposed that the origin of the irreversible capacity in amorphous  $\text{TiO}_2$  is the entrapment of  $\text{Li}^+$  in the low-energy sites during the early stages of lithiation (i.e., during pre-lithiation).

Lithiation in amorphous  $\text{TiO}_2$  starts by filling of the low-energy insertion sites, which makes  $\text{Li}^+$  relatively immobile due to the large  $U_{\text{m}}^{\text{b}}$  requirements for  $\text{Li}^+$  jump. Higher-energy insertion sites are then gradually filled by  $\text{Li}^+$  migration via lower  $U_{\text{m}}^{\text{b}}$  jumps. Consequently, the overall  $\text{Li}^+$  diffusion coefficient is expected to increase with increasing  $x$ . This explanation is supported by the experimental observations of Yildirim et al. that suggested that the  $U_{\text{m}}^{\text{b}}$  decreases with progressive lithiation.<sup>75</sup> This is in contrast to the effect on crystalline  $\text{TiO}_2$ , in which the diffusivity is expected to decrease with increasing  $x$  due to the limited availability of empty sites for Li accommodation and increasing Li–Li repulsion.

A compilation of previously reported values of diffusion coefficients for  $\text{Li}^+$  in  $\text{TiO}_2$  (from both theoretical and experimental studies) is presented in Table 1, and more detailed information on the energy barrier for  $\text{Li}^+$  diffusion at different  $x$  is presented in Table S4 (Supporting Information). The approximation of  $\nu^* = 10^{12}$  Hz<sup>60</sup> from Koudriachova et al. and  $\nu^* = 10^{13}$  Hz<sup>64</sup> from Tielens et al. were used to calculate  $D$  of  $\text{Li}^+$  at 300 K analytically using the  $U_{\text{m}}^{\text{b}}$  from previous studies.

**Table 1.** Diffusion Coefficient of  $\text{Li}^+$  at 300 K in Bulk Anatase, Rutile, and Amorphous  $\text{TiO}_2$

structure	$D$ ( $\text{cm}^2 \text{s}^{-1}$ )		
	this study	simulation	experiment
anatase	$x = 0.0278$ :	$x = 0.25$ : $5.39 \times 10^{-1159}$ <sup>a</sup>	$10^{-10}$ to $10^{-1779,80}$
	$1.17 \times 10^{-11}$	$x = 0.25$ : $5.25 \times 10^{-1275}$	
		$x = 1.0$ : $1.02 \times 10^{-1075}$	
	<b>c-axis at</b> $x = 0.0417$ :	<b>c-axis:</b>	<b>c-axis, <math>T = 823</math> K:</b>
rutile	$7.14 \times 10^{-4}$	$x = 0.5$ : $3.19 \times 10^{-559,a}$	$2.7 \times 10^{-382}$
		$x = 0.0417$ : $9.1 \times 10^{-681}$	
		$x = 0.0025$ : $9.3 \times 10^{-551}$	
	<b>basal at</b> $x = 0.0417$ :	<b>basal:</b>	
	$2.69 \times 10^{-37}$	$x = 0.5$ : $5.81 \times 10^{-3659}$ <sup>a</sup>	
amorphous	$U_{\text{m}}^{\text{b}} = 0.074$ , $x = 0.0625$ :	$x = 0.25$ : $2.35 \times 10^{-1775}$	$3.5 \times 10^{-1278}$
	$2.22 \times 10^{-5b}$	$x = 1.0$ : $1.36 \times 10^{-975}$	
	$2.22 \times 10^{-4c}$		
	$U_{\text{m}}^{\text{b}} = 0.744$ , $x = 0.0625$ :		
	$1.23 \times 10^{-16b}$		
	$1.23 \times 10^{-16c}$		

<sup>a</sup> $\nu^* = 10^{12}$  Hz was used. <sup>b</sup> $\nu^* = 10^{12}$  Hz,  $g = 1$ ,  $l = 3.42$  Å, and  $\alpha = 3$  were used. <sup>c</sup> $\nu^* = 10^{13}$  Hz,  $g = 1$ ,  $l = 3.42$  Å, and  $\alpha = 3$  were used.

**3.3.2. Insertion and Extraction of  $\text{Li}^+$  at the Electrolyte/ $\text{TiO}_2$  Interface.** This investigation focused on  $\text{Li}^+$  migration between the surface and the first layer to provide insight into  $\text{Li}^+$  insertion ( $U_{\text{m}}^{\text{i}}$ ) and  $\text{Li}^+$  extraction ( $U_{\text{m}}^{\text{e}}$ ) energy barriers. Under the assumption that the  $\text{TiO}_2$  electrode is already charge-stabilized following the arrival of  $\text{Li}^+$  on the surface (see Figure S5, Supporting Information), no correction of energy due to charge fluctuations in the electrode was required. Figure 9a–c shows the migration pathways of  $\text{Li}^+$ EC approaching the (001) anatase, (001) rutile, and amorphous  $\text{TiO}_2$  electrode surfaces with no pre-existing  $\text{Li}^+$  in  $\text{TiO}_2$  (i.e., assuming a pristine de-lithiated condition). The  $\text{Li}^+$ EC solvated complexes arrange differently at the interface as a result of different arrangements of surface atoms in the anatase, rutile, and amorphous  $\text{TiO}_2$ . In this study, (001) surfaces were assumed for both anatase and rutile. In anatase,  $\text{Li}^+$  diffusion is isotropic, and therefore, the influence of crystallographic orientations is less likely to be significant. However, for rutile, where  $\text{Li}^+$  diffusion is anisotropic, the (001) crystallographic surface was assumed as the migration direction from the surface to the bulk coincides with the fastest  $\text{Li}^+$  migration pathway via the  $c$ -axis.<sup>83</sup> Figure 9d depicts the minimum energy path for  $\text{Li}^+$  migration across the surface (EC/ $\text{TiO}_2$  interface) and into the first layer of  $\text{TiO}_2$ . In Figure 9d, the first peak showing  $U_{\text{m}}^{\text{i}}$  and  $U_{\text{m}}^{\text{e}}$  for the migration of  $\text{Li}^+$  between the surface and first layer of  $\text{TiO}_2$  is comparable with the second peak (in the shaded region) showing  $U_{\text{m}}^{\text{b}}$  for the diffusion of  $\text{Li}^+$  inside the bulk along the same direction, as calculated in Section 3.4. There are a total of four  $\text{Li}^+$  migration paths at the interface of amorphous  $\text{TiO}_2$  considered here; however, only one representative path is shown in Figure 9d.

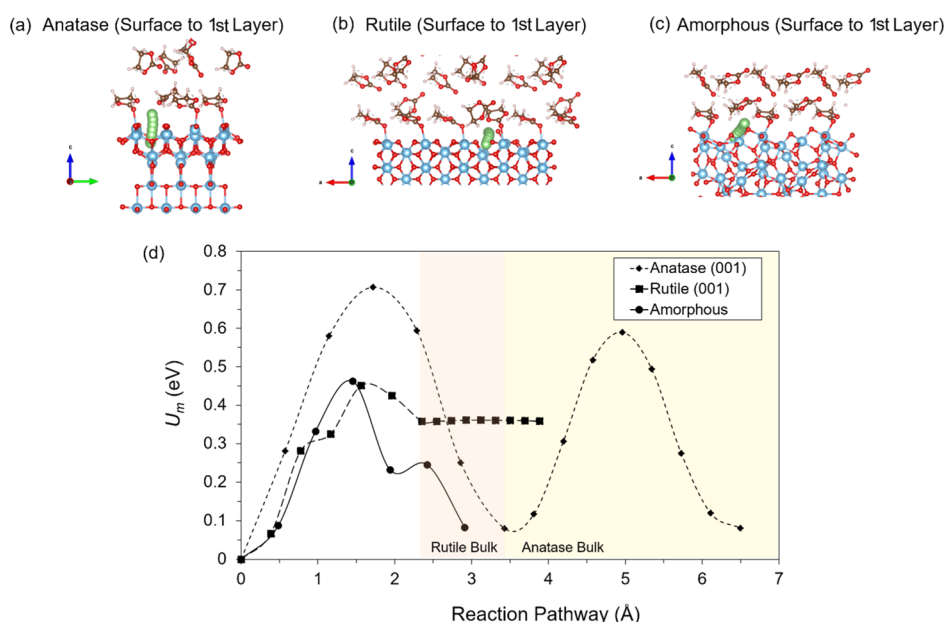


**Figure 9.** Migration pathways of  $\text{Li}^+$  (depicted by the green atoms) from the  $\text{TiO}_2$  surface to the first layer for anatase (a), rutile (b), and amorphous (c). (d)  $U_m$  for  $\text{Li}^+$  insertion (left to right) and  $\text{Li}^+$  extraction (right to left) at the EC/ $\text{TiO}_2$  interface. The shaded regions depict the  $\text{Li}^+$  migration energy barrier in the bulk  $\text{TiO}_2$ , as calculated in Section 3.4.

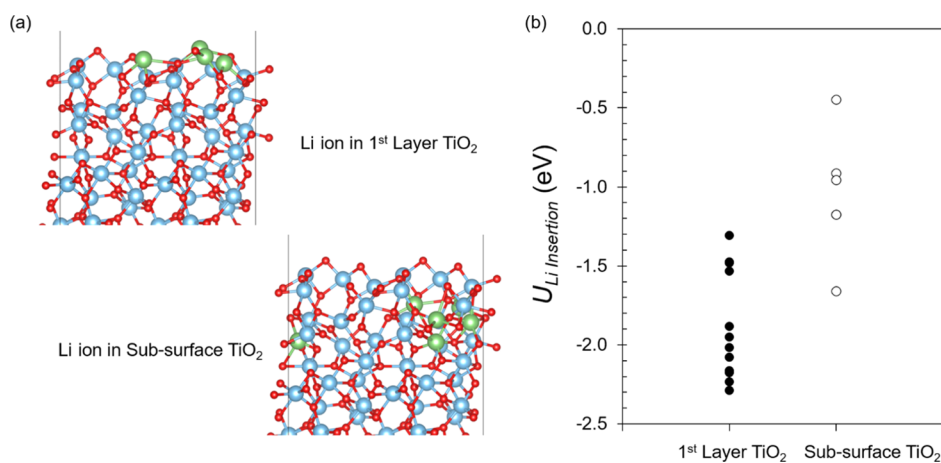


**Figure 10.** (a) Lithium-ion insertion on the surface and in the sub-surface layers of amorphous  $\text{TiO}_2$  and (b) their corresponding  $U_{\text{Li Insertion}}$  at different sites.

The insertion of  $\text{Li}^+$  from anatase and rutile  $\text{TiO}_2$  surfaces at the well-defined sites of 4b and 4c to the first layer requires  $U_m^i$  of 0.707 and 0.451 eV, whereas the extraction of  $\text{Li}^+$  from the first layer requires  $U_m^e$  of 0.627 and 0.093 eV, respectively. Compared to the experimental results, the energy barriers for  $\text{Li}^+$  migration across the interface of the chemically vapor-deposited anatase  $\text{TiO}_2$  film and nanoporous anatase  $\text{TiO}_2$  film electrodes have been reported to be between 0.54 and 0.35 eV for  $\text{Li}^+$  insertion and 0.78 and 0.38 eV for  $\text{Li}^+$  extraction.<sup>84</sup> Lithium-ion transport at the interface is sensitive to the crystallographic orientation and/or the arrangement of diffusion channels extending from the surface, such as those discussed above. In addition, the lower energy barrier calculated for extraction than for insertion may arise due to the use of  $\text{TiO}_2$  electrode models with low  $x$ . Comparative experimental values have been obtained from electrochemical experiments where samples were lithiated or de-lithiated for up to 30 min before the measurement.<sup>84</sup> This would have resulted

in larger and undefined values of  $x$ . In this study, the assumption of low  $x$  implied that interactions between neighboring  $\text{Li}^+$  were not captured, resulting in the energy barrier for de-lithiation being lower than the energy barrier for lithiation.

In amorphous  $\text{TiO}_2$ , similar to the situation for bulk diffusion, a wide range of  $U_{\text{Li Insertion}}$  values was observed near the surface, as shown in Figure 10. The  $U_{\text{Li Insertion}}$  in the first layer of amorphous  $\text{TiO}_2$  varies between  $-1.306$  and  $-2.287$  eV, while in the sub-surface layer, it ranges from  $-0.448$  to  $-1.660$  eV. Due to the limitations of the supercell size in the periodic boundary condition, the present study considers only four different  $\text{Li}^+$  migration pathways between the surface and first layer. The insertion of  $\text{Li}^+$  from the amorphous  $\text{TiO}_2$  surface to the first layer occurs with  $U_m^i$  ranging from 0.242 to 0.462 eV, whereas the extraction of  $\text{Li}^+$  to the surface requires  $U_m^e$  ranging from 0.146 to 0.351 eV. The highly disordered structure of amorphous  $\text{TiO}_2$  can lead to increased rate

capability, where  $\text{Li}^+$  migration at the interface and in the bulk is not confined into a certain path such as that in a crystalline structure. There are many non-equivalent sites available to host  $\text{Li}^+$  insertion in amorphous  $\text{TiO}_2$ . This is evidenced from a wide range of lithiation and de-lithiation potentials. Experimentally, this is reflected in broad lithiation and de-lithiation peaks during CV measurements.<sup>27,32</sup>

**3.4. Insertion and Extraction of  $\text{Li}^+$  in  $\text{TiO}_2$  as Functions of  $\Delta E$  and  $x$ .** Charge transfer is assumed to occur at the surface when a  $\text{Li}^+$  is inserted/extracted into the  $\text{TiO}_2$  accompanied by the concomitant reduction/oxidation of  $\text{Ti}^{4+}/\text{Ti}^{3+}$ . Using the implicit treatment of applied potential ( $\Delta E$ ) discussed in Section 2, the changes in  $U_A^i(\Delta E)$  and  $U_A^e(\Delta E)$  can be described using eqs 10a and 10b. Previous reports suggest that the applied potential across a  $\text{TiO}_2$  half-cell will induce a substantial  $\Delta E$  at the interface due to electronic conduction being faster than ionic conduction.<sup>85–87</sup> This applied potential is also expected to alter the arrangement of solvent molecules at the interface and thus also the migration of  $\text{Li}^+$  to the surface.<sup>88,89</sup> However, the influence of applied potential on the arrangement of solvent molecules at the surface was not treated explicitly (i.e., by applying an electric field in the calculations) as this study only considered the migration of  $\text{Li}^+$  between the surface and first layer of the different forms of  $\text{TiO}_2$ .

From the  $U_m^b$  calculated in Section 3.3.1 on  $\text{Li}^+$  diffusion in the bulk  $\text{TiO}_2$  and  $U_m^i$  and  $U_m^e$  in Section 3.3.2 on  $\text{Li}^+$  migration at the interface, the competing reactions of  $\text{Li}^+$  transport as a function of  $\Delta E$  can be determined. The estimations of  $U_m$  for  $\text{Li}^+$  insertion and extraction and in the bulk are summarized in Table 2, along with their jump lengths.

**Table 2. Migration Energy Barrier and Length for  $\text{Li}^+$  Insertion, Extraction, and Diffusion in  $\text{TiO}_2$**

pathways	migration energy barrier, $U_m$ (eV)		length <sup>a</sup> (Å)
	insertion	extraction	
Anatase $\text{TiO}_2$			
surface to the first layer	0.707	0.627	3.43
bulk (zigzag)	0.509	0.509	3.07
Rutile $\text{TiO}_2$			
surface to the first layer	0.451	0.093	2.35
bulk (c-axis)	0.004	0.004	1.48
bulk (basal)	2.013	2.013	3.30
Amorphous $\text{TiO}_2$			
surface to the first layer	0.242–0.408	0.146–0.351	2.29–4.27
bulk	0.074–0.744	0.074–0.744	0.50–4.48

<sup>a</sup>Note: migration length is calculated as the one-dimensional distance between the initial and final positions of  $\text{Li}^+$  in the structure.

Figure 11 shows the influences of  $\Delta E$  and  $x$  on the energy barrier ( $U_A(\Delta E)$ ) for  $\text{Li}^+$  migration at the interface and in the bulk. Although a full understanding on the rate-limiting step during lithiation/de-lithiation cannot be captured due to the complexity of predicting the changes in  $\text{Li}^+$  concentration, the competing behavior between surface and bulk reactions can still be rationalized. The differences of  $U_A(\Delta E)$  between surface and bulk processes can be used to understand the limiting reaction during the early stage of lithiation and de-lithiation (with pristine  $\text{TiO}_2$ ). The calculated barriers for  $\text{Li}^+$  insertion and extraction are limited to cases where a phase transformation does not occur. The calculated energy barriers

for  $\text{Li}^+$  diffusion in the bulk regions of the electrode at various  $x$  are valid only when  $\text{Li}_x\text{TiO}_2$  is homogeneous. It was shown that the  $D$  values of  $\text{Li}^+$  in anatase and rutile  $\text{TiO}_2$  decrease with increasing  $x$ , while in amorphous  $\text{TiO}_2$ , the value of  $D$  increases<sup>75,81</sup> (see Table S4, Supporting Information). Therefore, in Figure 11, the  $U_m^b$  for  $\text{Li}^+$  diffusion in anatase and rutile will increase with increasing  $x$ , whereas the  $U_m^b$  for  $\text{Li}^+$  diffusion in amorphous will decrease following the accumulation of  $\text{Li}^+$  in the bulk.

From Figure 11, it is shown that the dominant reaction at the interface is  $\text{Li}^+$  insertion during negatively applied potentials and  $\text{Li}^+$  extraction during positively applied potentials. These trends are as expected as lithiation occurs at a lower  $E$  than the de-lithiation. For anatase, at the  $E_{\text{onset}}$   $\text{Li}^+$  insertion into, and extraction from, the electrode have slightly higher  $U_m^i$  and  $U_m^e$  than  $U_m^b$  for  $\text{Li}^+$  diffusion in the bulk, as shown in Figure 11a, suggesting that the limiting reaction in the absence of applied potential using pristine anatase  $\text{TiO}_2$  is the surface process. Once  $\text{Li}^+$  inserts into anatase, it will easily diffuse into the bulk. However, the bulk diffusion of  $\text{Li}^+$  becomes the limiting reaction in a prolonged lithiation since the diffusion becomes slower with the accumulation of  $\text{Li}^+$  in the crystalline structure due to Li–Li repulsion.

For rutile  $\text{TiO}_2$ , at the  $E_{\text{onset}}$   $\text{Li}^+$  insertion into the electrode surface has a higher  $U_m^i$  than  $U_m^b$  (along the  $c$ -axis), suggesting that lithiation in pristine rutile  $\text{TiO}_2$  is also limited by the surface process (see Figure 11b). Diffusion along the basal plane can be neglected when considering insertion across the (001) surface since (i) it does not contribute to the  $\text{Li}^+$  insertion from the surface to the bulk and (ii) it is kinetically restricted (high  $U_m$ ) due to mechanical strains along the basal plane.<sup>71</sup> With increasing  $x$ , the lithiation and de-lithiation become limited by the bulk diffusion of  $\text{Li}^+$  as the value of  $U_m^b$  increases with increasing Li–Li repulsion.

In crystalline anatase and rutile  $\text{TiO}_2$ , the limiting factor in the early stages of lithiation and de-lithiation is the insertion of  $\text{Li}^+$  at the interface. Following the increase of  $x$  in crystalline  $\text{TiO}_2$ , the deceleration of  $\text{Li}^+$  diffusion in the bulk is expected as anatase and rutile have well-defined  $\text{Li}^+$  insertion sites that were occupied by  $\text{Li}^+$ , causing subsequent  $\text{Li}^+$  jumps to occur with a larger energy barrier due to increasing Li repulsion forces or limited to particular unoccupied sites. The use of electrodes comprising nano-sized  $\text{TiO}_2$  is beneficial to reduce the negative effect of Li repulsion as well as the segregation between Li-rich and Li-poor regions, minimizing the contribution of the  $\text{Li}^+$  bulk storage mechanism and maximizing the contribution of the  $\text{Li}^+$  surface storage mechanism in crystalline  $\text{TiO}_2$ .

In the case of amorphous  $\text{TiO}_2$ , there exists a range of values for  $U_m$ , which are represented in Figure 11c as shaded regions. First, variations in the values of  $U_A^i(\Delta E)$  and  $U_A^e(\Delta E)$  are due to variations of  $E_{\text{onset}}$  obtained from the Gibbs energy for  $\text{Li}^+$  insertion into the vacant non-equivalent sites in amorphous  $\text{TiO}_2$ . Second, the values of  $U_m^b$ ,  $U_A^i(\Delta E)$ , and  $U_A^e(\Delta E)$  also vary depending on the availability of active sites for  $\text{Li}^+$  insertion. It is revealed that  $\text{Li}^+$  insertion and extraction in amorphous  $\text{TiO}_2$  are not entirely dominated by the surface process but by the bulk process as well. However,  $\text{Li}^+$  diffusion in the bulk is predicted to increase with increasing  $x$  due to the occupation of  $\text{Li}^+$  insertion sites with low energy, leaving only sites with high  $U_{\text{Li Insertion}}$  that require a relatively lower  $U_m^b$ , such as those shown in Figure 8. The occupancy of  $\text{Li}^+$  sites with low energy also results in a significant amount of

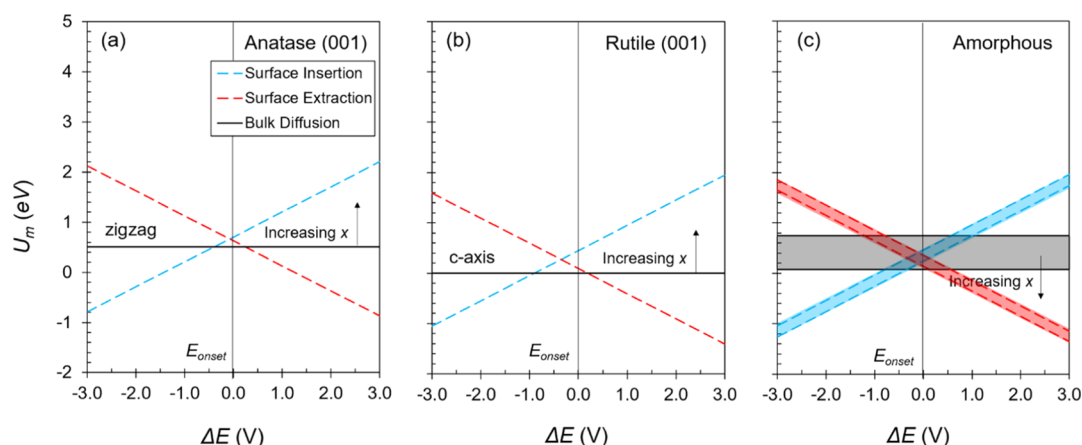


**Figure 11.** Energy barrier for  $\text{Li}^+$  migration in (a) anatase, (b) rutile, and (c) amorphous  $\text{TiO}_2$  electrodes as a function of  $\Delta E$ . Blue and red dashed lines represent  $\text{Li}^+$  insertion and extraction at the interface, respectively, and black solid lines represent the  $\text{Li}^+$  diffusion in the bulk. Shaded regions represent the distribution of  $U_m$  for  $\text{Li}^+$  migration in amorphous  $\text{TiO}_2$ .

irreversible capacity in amorphous  $\text{TiO}_2$ . In later stages of insertion and extraction (i.e., larger  $x$ ), lithiation and delithiation of amorphous  $\text{TiO}_2$  are not limited by bulk diffusion but more by the surface insertion/extraction process. Interfacial insertion/extraction in amorphous  $\text{TiO}_2$  can occur at lower  $U_A(\Delta E)$  than that in crystalline anatase and rutile  $\text{TiO}_2$  (see Table 2). This highlights that amorphous  $\text{TiO}_2$  may be suitable for high-rate applications.

The limiting factor in the early stage of lithiation and delithiation in the amorphous  $\text{TiO}_2$  electrode is bulk diffusion. With increasing  $x$ , the migration of  $\text{Li}^+$  in the bulk is accelerated as the low-energy  $\text{Li}^+$  insertion sites (i.e.,  $\text{Li}^+$  trapping sites) are progressively filled, leaving only the higher-energy sites, with higher associated mobility. The creation of new sites for  $\text{Li}^+$  diffusion pathways with lower energy barriers is also expected to occur in amorphous  $\text{TiO}_2$ <sup>75</sup> due to its flexible structure. It is important to note that even though the amorphous  $\text{TiO}_2$  surface enables rapid interfacial charge transfer, amorphous  $\text{TiO}_2$  is also capable of supporting bulk  $\text{Li}^+$  storage.<sup>32</sup>

#### 4. CONCLUSIONS

This study provides a comparative insight into  $\text{Li}^+$  storage in anatase, rutile, and amorphous  $\text{TiO}_2$  to explain the origin of improved capacity, rate capability, and cycling performance of nanostructured  $\text{TiO}_2$  battery anodes. A combination of empirical MD and DFT static atomic simulations was used to develop amorphous  $\text{TiO}_2$  models which were then used to compare  $\text{Li}^+$  insertion, extraction, and diffusion in amorphous, anatase, and rutile  $\text{TiO}_2$  both at the interface and in the bulk under an applied potential. DFT was used to predict the occurrence of phase transformations and structural evolution in  $\text{TiO}_2$  polymorphs due to progressive lithiation as well as the changes in  $\text{TiO}_2$  electrode potentials.

Lithium insertion in amorphous  $\text{TiO}_2$  exhibits a wide range of energies with a strong dependence on the neighboring Li–O, Li–Ti, and Li–Li atomic separations. In amorphous materials, the chemical pair interactions are critical for defining the  $\text{Li}^+$  insertion site energy and bulk  $\text{Li}^+$  migration energy barrier, which are found to be negatively correlated. This is contrary to the crystalline anatase and rutile  $\text{TiO}_2$  which exhibit a positive correlation between them. Due to large variations of chemical pair interactions in the structure,

lithiation of amorphous  $\text{TiO}_2$  is achieved at a range of potentials as there are no equivalent sites during  $\text{Li}^+$  insertion at the interface. This is reflected in the broad lithiation peaks observed using CV measurements.

A combination of surface and bulk storage mechanisms is shown in amorphous  $\text{TiO}_2$  due to the availability of sites that can accommodate  $\text{Li}^+$  with different migration and insertion energy characteristics. This results in the diffusion of  $\text{Li}^+$  occurring at an increasing rate with the increase of  $x$  as the low-energy  $\text{Li}^+$  sites become irreversibly filled. This differs from what is predicted to occur in anatase and rutile  $\text{TiO}_2$ , where the diffusion of  $\text{Li}^+$  occurs at a decreasing rate and is limited by the bulk storage mechanism with the increase of  $x$ . The use of nanostructures in crystalline  $\text{TiO}_2$  increases the  $\text{Li}^+$  surface storage capacity and reduces the dependence of electrode capacity on bulk storage of  $\text{Li}^+$ . This can improve the rate performance of electrodes comprising crystalline  $\text{TiO}_2$ .

Amorphous  $\text{TiO}_2$  is believed to possess a higher capacity than the crystalline forms of  $\text{TiO}_2$  with a larger volume expansion following lithiation. The benefits of nanostructuring for amorphous  $\text{TiO}_2$  are limited to (i) increasing the electrolyte/electrode surface area, thus enabling higher-rate charging and discharging and (ii) reduced volume expansion due to minimum contribution of the  $\text{Li}^+$  bulk storage mechanism.

#### ■ ASSOCIATED CONTENT

##### Supporting Information

The Supporting Information is available free of charge at <https://pubs.acs.org/doi/10.1021/acsami.0c17097>.

Atomistic models of bulk and surface calculations, lithium-ion configurations in  $\text{TiO}_2$  polymorphs using SOD, charge distribution of  $\text{Li}^+$  across the EC/ $\text{TiO}_2$  interface, diffusion of  $\text{Li}^+$  in  $\text{TiO}_2$ , and correlation between  $\text{Li}^+$  insertion energy and structural parameters in  $\text{Li}_x\text{TiO}_2$  (PDF)

#### ■ AUTHOR INFORMATION

##### Corresponding Author

Jodie A. Yuwono – School of Photovoltaic and Renewable Energy Engineering, UNSW Sydney, Kensington, New South Wales 2052, Australia; [orcid.org/0000-0002-0915-0756](https://orcid.org/0000-0002-0915-0756); Email: [j.yuwono@unsw.edu.au](mailto:j.yuwono@unsw.edu.au)

## Authors

**Patrick Burr** – School of Mechanical and Manufacturing Engineering, UNSW Sydney, Kensington, New South Wales 2052, Australia; [orcid.org/0000-0003-4796-9110](https://orcid.org/0000-0003-4796-9110)

**Conor Galvin** – School of Mechanical and Manufacturing Engineering, UNSW Sydney, Kensington, New South Wales 2052, Australia

**Alison Lennon** – School of Photovoltaic and Renewable Energy Engineering, UNSW Sydney, Kensington, New South Wales 2052, Australia

Complete contact information is available at:  
<https://pubs.acs.org/10.1021/acsami.0c17097>

## Author Contributions

The manuscript was written through contributions of J.A.Y., P.B., and A.L. C.G. was involved in the development of amorphous TiO<sub>2</sub> structures from MD simulations. All authors have given approval to the final version of the manuscript.

## Notes

The authors declare no competing financial interest.

## ACKNOWLEDGMENTS

This work was supported by the Australian Research Council through DP170103219 “Advanced Electrochemical Capacitors” and FT170100447. This work was undertaken with the assistance of resources and services from the National Computational Infrastructure (NCI) and the Pawsey Supercomputing Centre, which are supported by Australian Government and the Government of Western Australia, the UNSW Katana Supercomputing Cluster (Sydney, NSW), and was enabled by Intersect Australia Limited.

## REFERENCES

- (1) Pomerantseva, E.; Bonaccorso, F.; Feng, X.; Cui, Y.; Gogotsi, Y. Energy Storage: The Future Enabled by Nanomaterials. *Science* **2019**, *366*, No. eaan8285.
- (2) Lennon, A.; Jiang, Y.; Hall, C.; Lau, D.; Song, N.; Burr, P.; Grey, C. P.; Griffith, K. J. High-Rate Lithium Ion Energy Storage to Facilitate Increased Penetration of Photovoltaic Systems in Electricity Grids. *MRS Energy Sustain.* **2019**, *6*, No. E2.
- (3) Tomaszewska, A.; Chu, Z.; Feng, X.; O’Kane, S.; Liu, X.; Chen, J.; Ji, C.; Endler, E.; Li, R.; Liu, L.; Li, Y.; Zheng, S.; Vetterlein, S.; Gao, M.; Du, J.; Parkes, M.; Ouyang, M.; Marinescu, M.; Offer, G.; Wu, B. Lithium-Ion Battery Fast Charging: A Review. *ETransportation* **2019**, *1*, 100011.
- (4) Zhang, S. S. Identifying Rate Limitation and a Guide to Design of Fast-Charging Li-Ion Battery. *Infomatics* **2019**, *2*, 942.
- (5) Guan, X.; Wang, A.; Liu, S.; Li, G.; Liang, F.; Yang, Y.-W.; Liu, X.; Luo, J. Controlling Nucleation in Lithium Metal Anodes. *Small* **2018**, *14*, 1801423.
- (6) Tallman, K. R.; Zhang, B.; Wang, L.; Yan, S.; Thompson, K.; Tong, X.; Thieme, J.; Kiss, A.; Marschilok, A. C.; Takeuchi, K. J.; Bock, D. C.; Takeuchi, E. S. Anode Overpotential Control Via Interfacial Modification: Inhibition of Lithium Plating on Graphite Anodes. *ACS Appl. Mater. Interfaces* **2019**, *11*, 46864–46874.
- (7) Takami, N.; Inagaki, H.; Tatebayashi, Y.; Saruwatari, H.; Honda, K.; Egusa, S. High-Power and Long-Life Lithium-Ion Batteries Using Lithium Titanium Oxide Anode for Automotive and Stationary Power Applications. *J. Power Sources* **2013**, *244*, 469–475.
- (8) Sun, X.; Radovanovic, P. V.; Cui, B. Advances in Spinel Li<sub>4</sub>Ti<sub>5</sub>O<sub>12</sub> Anode Materials for Lithium-Ion Batteries. *New J. Chem.* **2015**, *39*, 38–63.
- (9) Chen, S.; Xin, Y.; Zhou, Y.; Ma, Y.; Zhou, H.; Qi, L. Self-Supported Li<sub>4</sub>Ti<sub>5</sub>O<sub>12</sub> Nanosheet Arrays for Lithium Ion Batteries with

Excellent Rate Capability and Ultralong Cycle Life. *Energy Environ. Sci.* **2014**, *7*, 1924.

(10) Huang, S.; Zhang, L.; Lu, X.; Liu, L.; Sun, X.; Yin, Y.; Oswald, S.; Zou, Z.; Ding, F.; Schmidt, O. G. Tunable Pseudocapacitance in 3D TiO<sub>2</sub>-Delta Nanomembranes Enabling Superior Lithium Storage Performance. *ACS Nano* **2017**, *11*, 821–830.

(11) Aravindan, V.; Lee, Y.-S.; Yazami, R.; Madhavi, S. TiO<sub>2</sub> Polymorphs in ‘Rocking-Chair’ Li-Ion Batteries. *Mater. Today* **2015**, *18*, 345–351.

(12) Yan, X.; Wang, Z.; He, M.; Hou, Z.; Xia, T.; Liu, G.; Chen, X. TiO<sub>2</sub> Nanomaterials as Anode Materials for Lithium-Ion Rechargeable Batteries. *Energy Technol.* **2015**, *3*, 801–814.

(13) El-Deen, S. S.; Hashem, A. M.; Abdel Ghany, A. E.; Indris, S.; Ehrenberg, H.; Mauger, A.; Julien, C. M. Anatase TiO<sub>2</sub> Nanoparticles for Lithium-Ion Batteries. *Ionics* **2018**, *24*, 2925–2934.

(14) Moitzheim, S.; Balder, J. E.; Poodt, P.; Unnikrishnan, S.; De Gendt, S.; Vereecken, P. M. Chlorine Doping of Amorphous TiO<sub>2</sub> for Increased Capacity and Faster Li-Ion Storage. *Chem. Mater.* **2017**, *29*, 10007–10018.

(15) Steiner, D.; Auer, A.; Portenkirchner, E.; Kunze-Liebhäuser, J. The Role of Surface Films During Lithiation of Amorphous and Anatase TiO<sub>2</sub> Nanotubes. *J. Electroanal. Chem.* **2018**, *812*, 166–173.

(16) Chen, J.; Tao, H. B.; Liu, B. Unraveling the Intrinsic Structures That Influence the Transport of Charges in TiO<sub>2</sub> Electrodes. *Adv. Energy Mater.* **2017**, *7*, 1700886.

(17) Cai, Y.; Wang, H.-E.; Zhao, X.; Huang, F.; Wang, C.; Deng, Z.; Li, Y.; Cao, G.; Su, B.-L. Walnut-Like Porous Core/Shell TiO<sub>2</sub> with Hybridized Phases Enabling Fast and Stable Lithium Storage. *ACS Appl. Mater. Interfaces* **2017**, *9*, 10652–10663.

(18) Bratić, M.; Jugović, D.; Mitrić, M.; Cvjetičanin, N. Insertion of Lithium Ion in Anatase TiO<sub>2</sub> Nanotube Arrays of Different Morphology. *J. Alloys Compd.* **2017**, *712*, 90–96.

(19) Dylla, A. G.; Henkelman, G.; Stevenson, K. J. Lithium Insertion in Nanostructured TiO<sub>2</sub>(B) Architectures. *Acc. Chem. Res.* **2013**, *46*, 1104–1112.

(20) Lui, G.; Li, G.; Wang, X.; Jiang, G.; Lin, E.; Fowler, M.; Yu, A.; Chen, Z. Flexible, Three-Dimensional Ordered Macroporous TiO<sub>2</sub> Electrode with Enhanced Electrode–Electrolyte Interaction in High-Power Li-Ion Batteries. *Nano Energy* **2016**, *24*, 72–77.

(21) Wang, B.; Bai, Y.; Xing, Z.; Hulicova-Jurcakova, D.; Wang, L. Enhanced Performance of a Pillared TiO<sub>2</sub> Nanohybrid as an Anode Material for Fast and Reversible Lithium Storage. *ChemNanoMat* **2015**, *1*, 96–101.

(22) Hu, Y.-S.; Kienle, L.; Guo, Y.-G.; Maier, J. High Lithium Electroactivity of Nanometer-Sized Rutile TiO<sub>2</sub>. *Adv. Mater.* **2006**, *18*, 1421–1426.

(23) Wagemaker, M.; van de Krol, R.; Kentgens, A. P. M.; van Well, A. A.; Mulder, F. M. Two Phase Morphology Limits Lithium Diffusion in TiO<sub>2</sub> (Anatase): A <sup>7</sup>Li MAS NMR Study. *J. Am. Chem. Soc.* **2001**, *123*, 11454–11461.

(24) Wagemaker, M.; Kentgens, A. P. M.; Mulder, F. M. Equilibrium Lithium Transport between Nanocrystalline Phases in Intercalated TiO<sub>2</sub> Anatase. *Nature* **2002**, *418*, 397–399.

(25) Wagemaker, M.; Lützenkirchen-Hecht, D.; van Well, A. A.; Frahm, R. Atomic and Electronic Bulk Versus Surface Structure Lithium Intercalation in Anatase TiO<sub>2</sub>. *J. Phys. Chem. B* **2004**, *108*, 12456–12464.

(26) Patra, S.; Davoisne, C.; Bouyanfif, H.; Foix, D.; Sauvage, F. Phase Stability Frustration on Ultra-Nanosized Anatase TiO<sub>2</sub>. *Sci. Rep.* **2015**, *5*, 10928.

(27) Moitzheim, S.; De Gendt, S.; Vereecken, P. M. Investigation of the Li-Ion Insertion Mechanism for Amorphous and Anatase TiO<sub>2</sub> Thin-Films. *J. Electrochem. Soc.* **2019**, *166*, A1–A9.

(28) Zukalová, M.; Kalbáč, M.; Kavan, L.; Exnar, I.; Graetzel, M. Pseudocapacitive Lithium Storage in TiO<sub>2</sub>(B). *Chem. Mater.* **2005**, *17*, 1248–1255.

- (29) Lee, J. B.; Chae, O. B.; Chae, S.; Ryu, J. H.; Oh, S. M. Amorphous Vanadium Titanates as a Negative Electrode for Lithium-Ion Batteries. *J. Electrochem. Sci. Technol.* **2016**, *7*, 306–315.
- (30) Chae, O. B.; Kim, J.; Park, I.; Jeong, H.; Ku, J. H.; Ryu, J. H.; Kang, K.; Oh, S. M. Reversible Lithium Storage at Highly Populated Vacant Sites in an Amorphous Vanadium Pentoxide Electrode. *Chem. Mater.* **2014**, *26*, 5874–5881.
- (31) Fang, H.-T.; Liu, M.; Wang, D.-W.; Sun, T.; Guan, D.-S.; Li, F.; Zhou, J.; Sham, T.-K.; Cheng, H.-M. Comparison of the Rate Capability of Nanostructured Amorphous and Anatase TiO<sub>2</sub> for Lithium Insertion Using Anodic TiO<sub>2</sub> Nanotube Arrays. *Nanotechnology* **2009**, *20*, 225701.
- (32) Jiang, Y.; Hall, C.; Song, N.; Lau, D.; Burr, P. A.; Patterson, R.; Wang, D.-W.; Ouyang, Z.; Lennon, A. Evidence for Fast Lithium-Ion Diffusion and Charge-Transfer Reactions in Amorphous TiO<sub>x</sub> Nanotubes: Insights for High-Rate Electrochemical Energy Storage. *ACS Appl. Mater. Interfaces* **2018**, *10*, 42513–42523.
- (33) Wei, Z.; Wang, D.; Yang, X.; Wang, C.; Chen, G.; Du, F. From Crystalline to Amorphous: An Effective Avenue to Engineer High-Performance Electrode Materials for Sodium-Ion Batteries. *Adv. Mater. Interfac.* **2018**, *5*, 1800639.
- (34) Ku, J. H.; Ryu, J. H.; Kim, S. H.; Han, O. H.; Oh, S. M. Reversible Lithium Storage with High Mobility at Structural Defects in Amorphous Molybdenum Dioxide Electrode. *Adv. Funct. Mater.* **2012**, *22*, 3658–3664.
- (35) Shih, W. S.; Young, S. J.; Ji, L. W.; Water, W.; Shiu, H. W. TiO<sub>2</sub>-Based Thin Film Transistors with Amorphous and Anatase Channel Layer. *J. Electrochem. Soc.* **2011**, *158*, H609.
- (36) Kerisit, S.; Rosso, K. M.; Yang, Z.; Liu, J. Computer Simulation of the Phase Stabilities of Lithiated TiO<sub>2</sub> Polymorphs. *J. Phys. Chem. C* **2010**, *114*, 19096–19107.
- (37) Matsui, M.; Akaogi, M. Molecular Dynamics Simulation of the Structural and Physical Properties of the Four Polymorphs of TiO<sub>2</sub>. *Mol. Simul.* **1991**, *6*, 239–244.
- (38) Kresse, G.; Furthmüller, J. Efficiency of Ab-Initio Total Energy Calculations for Metals and Semiconductors Using a Plane-Wave Basis Set. *Comput. Mater. Sci.* **1996**, *6*, 15–50.
- (39) Kresse, G.; Furthmüller, J. Efficient iterative schemes for ab initio total-energy calculations using a plane-wave basis set. *Phys. Rev. B: Condens. Matter Mater. Phys.* **1996**, *54*, 11169–11186.
- (40) Perdew, J. P.; Burke, K.; Ernzerhof, M. Generalized Gradient Approximation Made Simple. *Phys. Rev. Lett.* **1996**, *77*, 3865–3868.
- (41) Blöchl, P. E. Projector Augmented-Wave Method. *Phys. Rev. B: Condens. Matter Mater. Phys.* **1994**, *50*, 17953–17979.
- (42) Kresse, G.; Joubert, D. From Ultrasoft Pseudopotentials to the Projector Augmented Wave Method. *Phys. Rev. B: Condens. Matter Mater. Phys.* **1999**, *59*, 1758–1775.
- (43) Grimme, S.; Antony, J.; Ehrlich, S.; Krieg, H. A Consistent and Accurate Ab Initio Parametrization of Density Functional Dispersion Correction (DFT-D) for the 94 Elements H-Pu. *J. Chem. Phys.* **2010**, *132*, 154104.
- (44) Moellmann, J.; Ehrlich, S.; Tonner, R.; Grimme, S. A DFT-D Study of Structural and Energetic Properties of TiO<sub>2</sub> Modifications. *J. Phys. Condens. Matter* **2012**, *24*, 424206.
- (45) Leung, K.; Tenney, C. M. Toward First Principles Prediction of Voltage Dependences of Electrolyte/Electrolyte Interfacial Processes in Lithium Ion Batteries. *J. Phys. Chem. C* **2013**, *117*, 24224–24235.
- (46) Cava, R. J.; Murphy, D. W.; Zahurak, S.; Santoro, A.; Roth, R. S. The Crystal Structures of the Lithium-Inserted Metal Oxides Li<sub>0.5</sub>TiO<sub>2</sub> Anatase, LiTi<sub>2</sub>O<sub>4</sub> Spinel, and Li<sub>2</sub>Ti<sub>2</sub>O<sub>4</sub>. *J. Solid State Chem.* **1984**, *53*, 64–75.
- (47) Cromer, D. T.; Herrington, K. The Structures of Anatase and Rutile. *J. Am. Chem. Soc.* **1955**, *77*, 4708–4709.
- (48) Pfanzelt, M.; Kubiak, P.; Fleischhammer, M.; Wohlfahrt-Mehrens, M. TiO<sub>2</sub> Rutile—an Alternative Anode Material for Safe Lithium-Ion Batteries. *J. Power Sources* **2011**, *196*, 6815–6821.
- (49) Vijayakumar, M.; Kerisit, S.; Wang, C.; Nie, Z.; Rosso, K. M.; Yang, Z.; Graff, G.; Liu, J.; Hu, J. Effect of Chemical Lithium Insertion into Rutile TiO<sub>2</sub> Nanorods. *J. Phys. Chem. C* **2009**, *113*, 14567–14574.
- (50) Grau-Crespo, R.; Hamad, S.; Catlow, C. R. A.; Leeuw, N. H. d. Symmetry-Adapted Configurational Modelling of Fractional Site Occupancy in Solids. *J. Phys.: Condens. Matter* **2007**, *19*, 256201.
- (51) Kerisit, S.; Rosso, K. M.; Yang, Z.; Liu, J. Dynamics of Couples Lithium/Electron Diffusion in TiO<sub>2</sub> Polymorphs. *J. Phys. Chem. C* **2009**, *113*, 20998–21007.
- (52) Rong, Z.; Kitchaev, D.; Canepa, P.; Huang, W.; Ceder, G. An Efficient Algorithm for Finding the Minimum Energy Path for Cation Migration in Ionic Materials. *J. Chem. Phys.* **2016**, *145*, 074112.
- (53) Milman, V.; Payne, M. C.; Heine, V.; Needs, R. J.; Lin, J. S.; Lee, M. H. Free Energy and Entropy of Diffusion by Ab Initio Molecular Dynamics: Alkali Ions in Silicon. *Phys. Rev. Lett.* **1993**, *70*, 2928–2931.
- (54) Vineyard, G. H. Frequency Factors and Isotope Effects in Solid State Rate Processes. *J. Phys. Chem. Solids* **1957**, *3*, 121–127.
- (55) Messina, L.; Nastar, M.; Sandberg, N.; Olsson, P. Systematic Electronic-Structure Investigation of Substitutional Impurity Diffusion and Flux Coupling in BCC Iron. *Phys. Rev. B* **2016**, *93*, 184302.
- (56) Berhaut, C. L.; Lemordant, D.; Porion, P.; Timperman, L.; Schmidt, G.; Anouti, M. Ionic Association Analysis of LiTDI, LiFSI and LiPF<sub>6</sub> in EC/DMC for Better Li-Ion Battery Performances. *RSC Adv.* **2019**, *9*, 4599–4608.
- (57) Lindström, H.; Södergren, S.; Solbrand, A.; Rensmo, H.; Hjelm, J.; Hagfeldt, A.; Lindquist, S.-E. Li<sup>+</sup> Ion Insertion in TiO<sub>2</sub> (Anatase). 2. Voltammetry on Nanoporous Films. *J. Phys. Chem. B* **1997**, *101*, 7717–7722.
- (58) Petkov, V.; Holzhüter, G.; Tröge, U.; Gerber, T.; Himmel, B. Atomic-Scale Structure of Amorphous TiO<sub>2</sub> by Electron, X-Ray Diffraction and Reverse Monte Carlo Simulations. *J. Non-Cryst. Solids* **1998**, *231*, 17–30.
- (59) Arrouel, C.; Peixoto, T. C.; Valerio, M. E. G.; Parker, S. C. Lithium Migration at Low Concentration in TiO<sub>2</sub> Polymorphs. *Comput. Theor. Chem.* **2015**, *1072*, 43–51.
- (60) Koudriachova, M. V.; Harrison, N. M.; de Leeuw, S. W. Effect of Diffusion on Lithium Intercalation in Titanium Dioxide. *Phys. Rev. Lett.* **2001**, *86*, 1275–1278.
- (61) Xiong, H.; Yildirim, H.; Shevchenko, E. V.; Prakapenka, V. B.; Koo, B.; Slater, M. D.; Balasubramanian, M.; Sankaranarayanan, S. K. R. S.; Greeley, J. P.; Tepavcevic, S.; Dimitrijevic, N. M.; Podsiadlo, P.; Johnson, C. S.; Rajh, T. Self-Improving Anode for Lithium-Ion Batteries Based on Amorphous to Cubic Phase Transition in TiO<sub>2</sub> Nanotubes. *J. Phys. Chem. C* **2012**, *116*, 3181–3187.
- (62) Yildirim, H.; Greeley, J. P.; Sankaranarayanan, S. K. R. S. Localized Order-Disorder Transitions Induced by Li Segregation in Amorphous TiO<sub>2</sub> Nanoparticles. *ACS Appl. Mater. Interfaces* **2014**, *6*, 18962–18970.
- (63) Yildirim, H.; Greeley, J. P.; Sankaranarayanan, S. K. R. S. Concentration-Dependent Ordering of Lithiated Amorphous TiO<sub>2</sub>. *J. Phys. Chem. C* **2013**, *117*, 3834–3845.
- (64) Tielens, F.; Calatayud, M.; Beltrán, A.; Minot, C.; Andrés, J. Lithium Insertion and Mobility in the TiO<sub>2</sub>-Anatase/Titanate Structure: A Periodic Dft Study. *J. Electroanal. Chem.* **2005**, *581*, 216–223.
- (65) Borghols, W. J. H.; Wagemaker, M.; Lafont, U.; Kelder, E. M.; Mulder, F. M. Impact of Nanosizing on Lithiated Rutile TiO<sub>2</sub>. *Chem. Mater.* **2008**, *20*, 2949–2955.
- (66) Liu, H.; Grey, C. P. Influence of Particle Size, Cycling Rate and Temperature on the Lithiation Process of Anatase TiO<sub>2</sub>. *J. Mater. Chem. A* **2016**, *4*, 6433–6446.
- (67) Christensen, C. K.; Mamakhel, M. A. H.; Balakrishna, A. R.; Iversen, B. B.; Chiang, Y.-M.; Ravnsbæk, D. B. Order-Disorder Transition in Nano-Rutile TiO<sub>2</sub> Anodes: A High Capacity Low-Volume Change Li-Ion Battery Material. *Nanoscale* **2019**, *11*, 12347–12357.
- (68) Jiang, C.; Honma, I.; Kudo, T.; Zhou, H. Nanocrystalline Rutile TiO<sub>2</sub> Electrode for High-Capacity and High-Rate Lithium Storage. *Electrochem. Solid-State Lett.* **2007**, *10*, A127.

- (69) Pfanzelt, M.; Kubiak, P.; Wohlfahrt-Mehrens, M. Nanosized TiO<sub>2</sub> Rutile with High Capacity and Excellent Rate Capability. *Electrochem. Solid-State Lett.* **2010**, *13*, A91.
- (70) Pfanzelt, M.; Kubiak, P.; Jacke, S.; Dimesso, L.; Jaegermann, W.; Wohlfahrt-Mehrens, M. Sei Formation on TiO<sub>2</sub> Rutile. *J. Electrochem. Soc.* **2012**, *159*, A809–A814.
- (71) Baudrin, E.; Cassaignon, S.; Koelsch, M.; Jolivet, J.; Dupont, L.; Tarascon, J. Structural Evolution During the Reaction of Li with Nano-Sized Rutile Type TiO<sub>2</sub> at Room Temperature. *Electrochem. Commun.* **2007**, *9*, 337–342.
- (72) Arrouvel, C.; Parker, S. C.; Islam, M. S. Lithium Insertion and Transport in the TiO<sub>2</sub>–B Anode Material: A Computational Study. *Chem. Mater.* **2009**, *21*, 4778–4783.
- (73) Lin, D.; Lu, Z.; Hsu, P.-C.; Lee, H. R.; Liu, N.; Zhao, J.; Wang, H.; Liu, C.; Cui, Y. A High Tap Density Secondary Silicon Particle Anode Fabricated by Scalable Mechanical Pressing for Lithium-Ion Batteries. *Energy Environ. Sci.* **2015**, *8*, 2371–2376.
- (74) Han, J.; Hirata, A.; Du, J.; Ito, Y.; Fujita, T.; Kohara, S.; Ina, T.; Chen, M. Intercalation Pseudocapacitance of Amorphous Titanium Dioxide@Nanoporous Graphene for High-Rate and Large-Capacity Energy Storage. *Nano Energy* **2018**, *49*, 354–362.
- (75) Yildirim, H.; Greeley, J.; Sankaranarayanan, S. K. R. S. Effect of Concentration on the Energetics and Dynamics of Li Ion Transport in Anatase and Amorphous TiO<sub>2</sub>. *J. Phys. Chem. C* **2011**, *115*, 15661–15673.
- (76) Olson, C. L.; Nelson, J.; Islam, M. S. Defect Chemistry, Surface Structures, and Lithium Insertion in Anatase TiO<sub>2</sub>. *J. Phys. Chem. B* **2006**, *110*, 9995–10001.
- (77) Koudriachova, M. Diffusion of Li-Ions in Rutile. An Ab Initio Study. *Solid State Ionics* **2003**, *157*, 35–38.
- (78) Borghols, W. J. H.; Lützenkirchen-Hecht, D.; Haake, U.; Chan, W.; Lafont, U.; Kelder, E. M.; van Eck, E. R. H.; Kentgens, A. P. M.; Mulder, F. M.; Wagemaker, M. Lithium Storage in Amorphous TiO<sub>2</sub> Nanoparticles. *J. Electrochem. Soc.* **2010**, *157*, A582.
- (79) Kavan, L.; Rathousky, J.; Gratzel, M.; Shklover, V.; Zukal, A. Surfactant-Templated TiO<sub>2</sub> (Anatase): Characteristic Features of Lithium Insertion Electrochemistry in Organized Nanostructures. *J. Phys. Chem. B* **2000**, *104*, 12012–12020.
- (80) Liu, Z.; Hong, L.; Guo, B. Physicochemical and Electrochemical Characterization of Anatase Titanium Dioxide Nanoparticles. *J. Power Sources* **2005**, *143*, 231–235.
- (81) Yildirim, H.; Greeley, J. P.; Sankaranarayanan, S. K. R. S. The Effect of Concentration on Li Diffusivity and Conductivity in Rutile TiO<sub>2</sub>. *Phys. Chem. Chem. Phys.* **2012**, *14*, 4565–4576.
- (82) Johnson, O. W. One-Dimensional Diffusion of Li in Rutile. *Phys. Rev.* **1964**, *136*, A284–A290.
- (83) Auer, A.; Portenkirchner, E.; Götsch, T.; Valero-Vidal, C.; Penner, S.; Kunze-Liebhäuser, J. Preferentially Oriented TiO<sub>2</sub> Nanotubes as Anode Material for Li-Ion Batteries: Insight into Li-Ion Storage and Lithiation Kinetics. *ACS Appl. Mater. Interfaces* **2017**, *9*, 36828–36836.
- (84) Lindström, H.; Södergren, S.; Solbrand, A.; Rensmo, H.; Hjelm, J.; Hagfeldt, A.; Lindquist, S.-E. Li<sup>+</sup> Ion Insertion in TiO<sub>2</sub> (Anatase). I. Chronoamperometry on Cvd Films and Nanoporous Films. *J. Phys. Chem. B* **1997**, *101*, 7710–7716.
- (85) Deskins, N. A.; Dupuis, M. Electron Transport Via Polaron Hopping in Bulk TiO<sub>2</sub>: A Density Functional Theory Characterization. *Phys. Rev. B: Condens. Matter Mater. Phys.* **2007**, *75*, 195212.
- (86) Pham, H. H.; Wang, L.-W. Oxygen Vacancy and Hole Conduction in Amorphous TiO<sub>2</sub>. *Phys. Chem. Chem. Phys.* **2015**, *17*, 541–550.
- (87) Nunez, P.; Richter, M. H.; Piercy, B. D.; Roske, C. W.; Cabán-Acevedo, M.; Losego, M. D.; Konezny, S. J.; Fermin, D. J.; Hu, S.; Brunshwig, B. S.; Lewis, N. S. Characterization of Electronic Transport through Amorphous TiO<sub>2</sub> Produced by Atomic Layer Deposition. *J. Phys. Chem. C* **2019**, *123*, 20116–20129.
- (88) Yuwono, J. A.; Birbilis, N.; Williams, K. S.; Medhekar, N. V. Electrochemical Stability of Magnesium Surfaces in an Aqueous Environment. *J. Phys. Chem. C* **2016**, *120*, 26922–26933.
- (89) Vasudevan, V.; Wang, M.; Yuwono, J. A.; Jasieniak, J.; Birbilis, N.; Medhekar, N. V. Ion Agglomeration and Transport in MgCl<sub>2</sub>-Based Electrolytes for Rechargeable Magnesium Batteries. *J. Phys. Chem. Lett.* **2019**, *10*, 7856–7862.